

# We are IntechOpen, the world's leading publisher of Open Access books Built by scientists, for scientists

6,900

Open access books available

186,000

International authors and editors

200M

Downloads

Our authors are among the

154

Countries delivered to

TOP 1%

most cited scientists

12.2%

Contributors from top 500 universities



WEB OF SCIENCE™

Selection of our books indexed in the Book Citation Index  
in Web of Science™ Core Collection (BKCI)

Interested in publishing with us?  
Contact [book.department@intechopen.com](mailto:book.department@intechopen.com)

Numbers displayed above are based on latest data collected.  
For more information visit [www.intechopen.com](http://www.intechopen.com)



---

## Focusing MSs for High-Gain Antenna Applications

---

Haipeng Li, Guangming Wang, Wenye Ji, Tong Cai,  
Xiangjun Gao and Haisheng Hou

Additional information is available at the end of the chapter

<http://dx.doi.org/10.5772/intechopen.79351>

---

### Abstract

Recently, metasurfaces (MSs) have continuously drawn significant attentions in the area of enhancing the performances of the conventional antennas. Thereinto, focusing MSs with hyperbolic phase distributions can be used for designing high-gain antennas. In this chapter, we first design a new reflected MS and use a spiral antenna as the feeding source to achieve a wideband high-gain antenna. On this basis, we propose a bi-layer reflected MS to simultaneously enhance the gain and transform the linear polarization to circular polarization of the Vivaldi antenna. Then, we proposed a multilayer transmitted MS and use it to enhance the gain of a patch antenna. This kind of high-gain antenna eliminates the feed-block effect of the reflected ones but suffer from multilayer fabrication. To conquer this problem, we finally propose a single-layer transmitted focusing MS by grouping two different kinds of elements and use it to successfully design a low-profile high-gain antenna.

**Keywords:** focusing, MS, high-gain antenna, reflection, transmission

---

### 1. Wideband reflected high-gain antenna based on single-layered focusing metasurface

In last several years, metasurface (MS) has become a research hotspot since it relieves the drawbacks of bulk metamaterials. An MS usually consists of a set of periodic or locally nonperiodic unit cells with subwavelength thickness. The phase gradient metasurface (PGMS) is a special kind of MS which has been proposed by Yu et al. to demonstrate the general Snell's law [1]. Since the PGMS is able to provide predefined in-plane wave vectors to manipulate the directions of the refracting/reflecting waves, it consequently attracts a lot attention in beam steering. In Ref. [1], the authors designed a PGMS by using nano-V-antennas with different shapes to verify anomalous reflection/refraction effects, which opens the door to the rapid

---

development of MS for beam steering. Over the last 5 years, the MS has ushered in the golden age of theoretical and practical researches. Many applications of MS have emerged in the areas of focusing [2–8], anomalous refraction/reflection [6, 7], surface-plasmon-polariton coupling [8, 9], radar cross section (RCS) reduction [10–12], and polarization manipulation [13]. Generally, a wide phase-steering range covering  $2\pi$  is an essential characteristic for the MS element. The phase is manipulated by changing the structure size or rotating the angle of the particle on the substrate. Then, by fixing proper phase distributions on the MS, we can flexibly manipulate the wavefronts and the polarizations of the EM waves. These characteristics as well as compact size and low loss mean the MS can be a good candidate to improve antenna performance by enhancing the antenna gain [4], reducing the RCS of the antenna [12], converting the antenna polarization [13]. We call this kind of high-performance antenna based on MS as MS antenna. Thereinto, the focusing MSs usually have been used to enhance the gain of the antenna. They can also transform spherical wave emitted by a point source placed at the focal point to plane wave theoretically. In such case, the directivity and gain of the point source can be improved greatly.

### 1.1. Theory

**Figure 1** depicts the schematic used to derive the generalized law of reflection. The introduction of an abrupt phase shift, denoted as phase discontinuity, at the interface between two media allows us to revisit the law of reflection by applying Fermat's principle. The incident angle of the electromagnetic wave is  $\theta_i$ . Assuming that the blue and red paths are infinitesimally close to the actual light path, then the phase difference between them is zero.

$$kn_i \sin(\theta_i) dx + \Phi + d\Phi - [kn_i \sin(\theta_r) dx + \Phi] = 0 \quad (1)$$

where  $\Phi$  is the phase discontinuity at a local position on the MS,  $n_i$  is the index of the incident medium, and  $\theta_r$  ( $\theta_i$ ) is the reflected (incident) angle of the electromagnetic wave. By insertion of  $k = 2\pi/\lambda$ , we can obtain the following generalized reflection Snell's law [1]:

$$\sin(\theta_r) - \sin(\theta_i) = \frac{\lambda}{2\pi n_i} \frac{d\Phi}{dx} \quad (2)$$

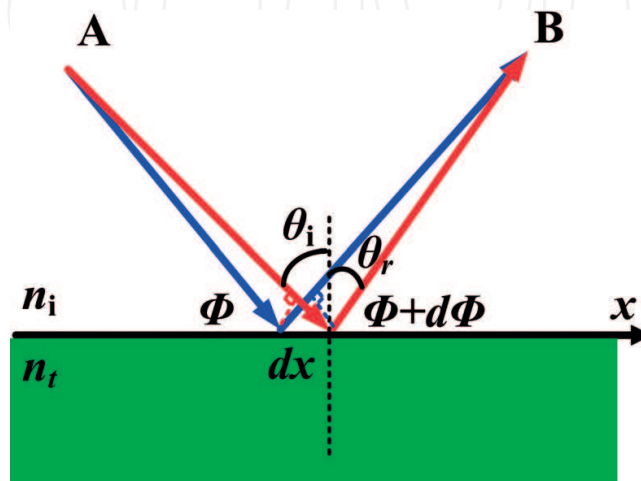


**Figure 1.** Schematic used to derive the generalized law of reflection.

As shown in **Figure 2(a)**, if the designed  $d\Phi/dx$  is a constant, anomalous reflection will be achieved, and the reflected angle can be controlled. The phase distribution of the focusing MS has to satisfy the following Eq. (3).

$$\varphi(x, y) = \frac{2\pi}{\lambda} (\sqrt{x^2 + y^2 + L^2} - L) + \varphi_1 \quad (3)$$

where  $L$  is the focal distance,  $\varphi_1$  is the phase shift through the first unit cell, which is placed at the point  $x = 0, y = 0$ . The MS can focus the incident plane wave to its focal point as shown in **Figure 2(b)**. Likewise, the sphere wave emitted by the source placed at its focal point can be converted to plane wave as shown in **Figure 2(c)**, which can be used for designing high-gain antennas.

## 1.2. Unit cell design

**Figure 3** shows the structure of the MS element, which is utilized to build the reflected MS. The top metallic layer is composed of a cross and a cross-ring (CCR), and the bottom layer is totally metal. The dielectric layer has a substrate with the permittivity of 2.65 and

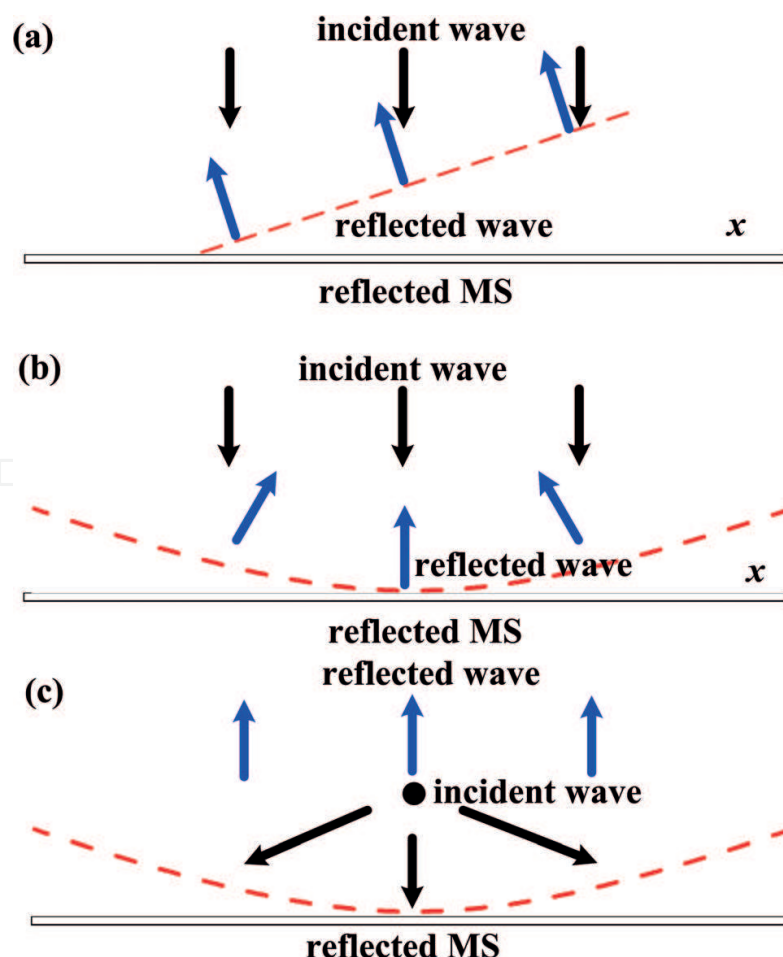


**Figure 2.** Schematics used to describe (a) anomalous reflection (b) focusing effect, and (c) operating mechanism of the MS antenna.



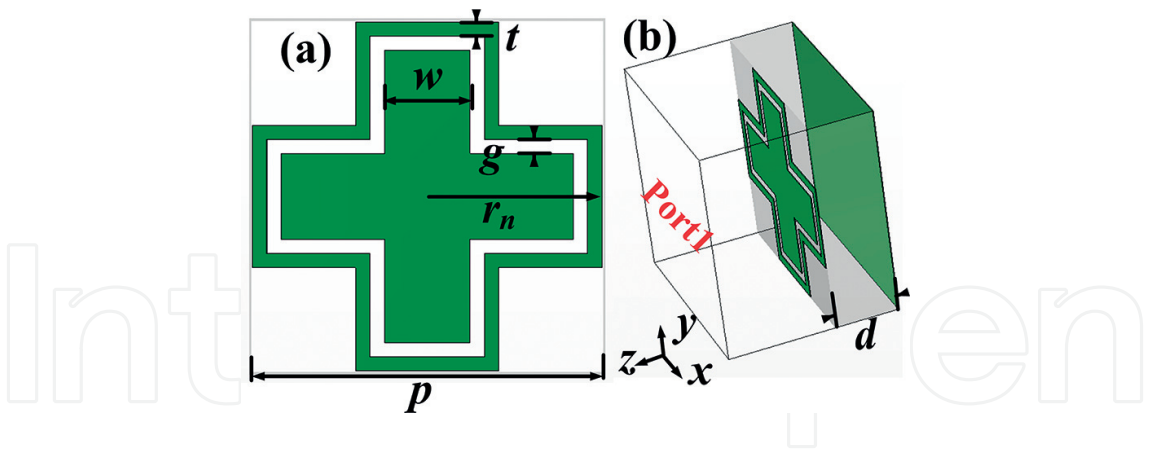


**Figure 3.** Structure of the MS element and the simulated setup. (a) Top view and (b) perspective view.  $w = 2.4$  mm,  $g = t = 0.4$  mm,  $p = 10$  mm,  $d = 3$  mm, and  $n = 1, 2, 3, \dots$

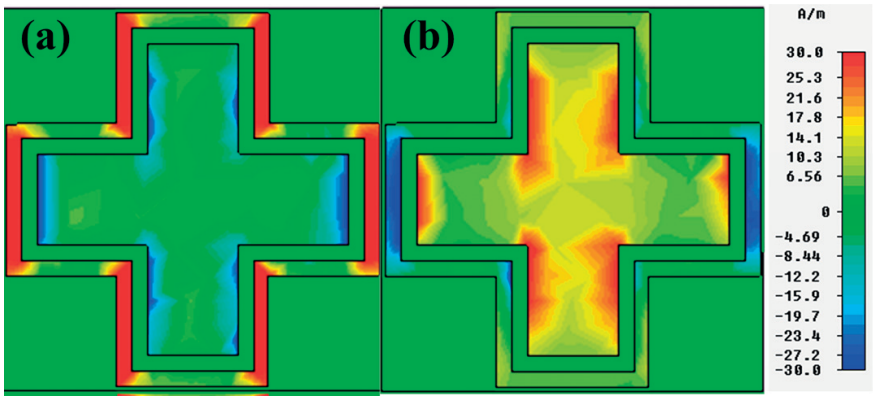


**Figure 4.** Current distribution on the upper surface of the CCR unit cell at (a) 4.5 GHz and (b) 9.5 GHz.

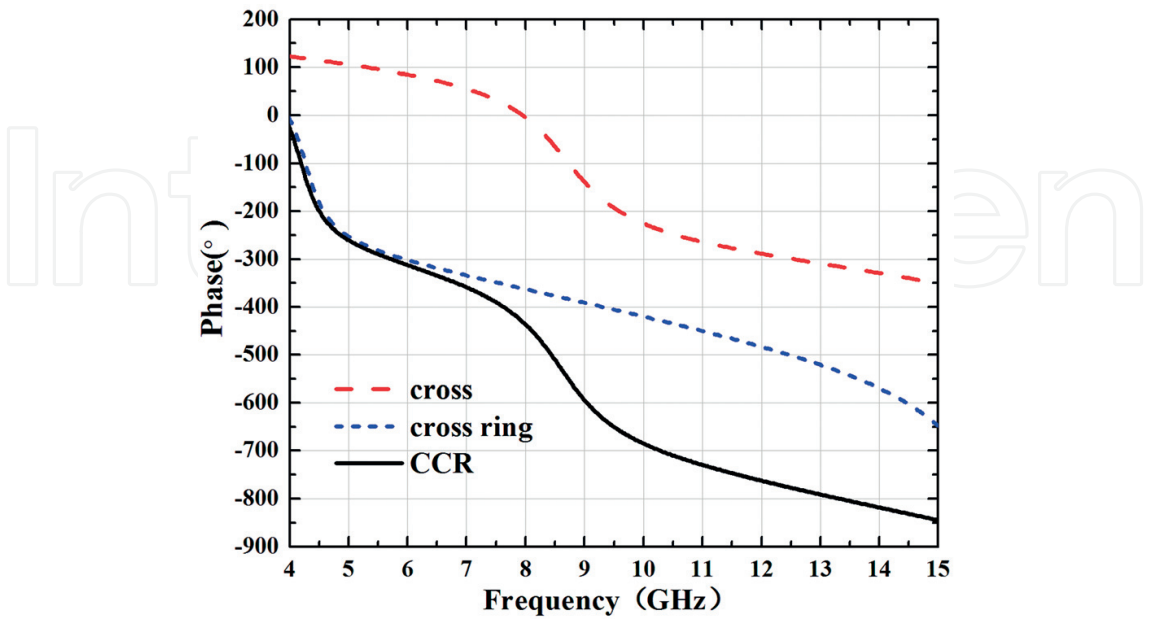


**Figure 5.** Phase of  $S_{11}$  for three different unit cells.

thickness of 3 mm. For characterization, the unit cell is simulated in CST Microwave Studio by using periodic boundary. To illustrate the operating mechanism of the CCR unit cell clearly, **Figure 4** shows the current distribution on the upper surface of the unit cell and **Figure 5** shows the phase of  $S_{11}$  in a broad frequency band. As shown in **Figure 5**, the phase of  $S_{11}$  changes fast around 4.5 and 9.5 GHz, which is the two resonances of the CCR unit cell. From **Figure 4**, it can be find that the lower resonant frequency (4.5 GHz) is brought by the cross-ring structure and the higher one is brought by the cross-structure. Due to the dual-resonance structure, the phase difference of the CCR unit cell has successfully reached about  $620^\circ$  just by changing the parameter of  $r_n$  as shown in **Figure 6**.

In addition, the curves in **Figure 7** have good linearity especially during 10–12 GHz, which makes the CCR unit cell very suitable for broadband design. To completely evaluate the reflected phase character of the unit cell, a parameter scan has been made with the step of 0.01 mm for  $r_n$  in CST, and curves of the reflected phase change with  $r_n$  (2 mm–4.9 mm) at 10, 11, and 12 GHz are shown in **Figure 10**. The three curves are almost parallel with each other, which guarantee that the phase distribution changes little with frequency during the range of 10–12 GHz.

### 1.3. Focusing metasurface antenna design

After successfully designing the required broadband unit cell, we use it to design the focusing MS. The reflected phase difference distribution in the plane which is perpendicular to the direction of the incident plane-wave should satisfy the profile mentioned in Eq. (3). The period of the CCR unit cell is  $p$ , so the location of the unit cell can be discretized as  $x = n \times p$ ,

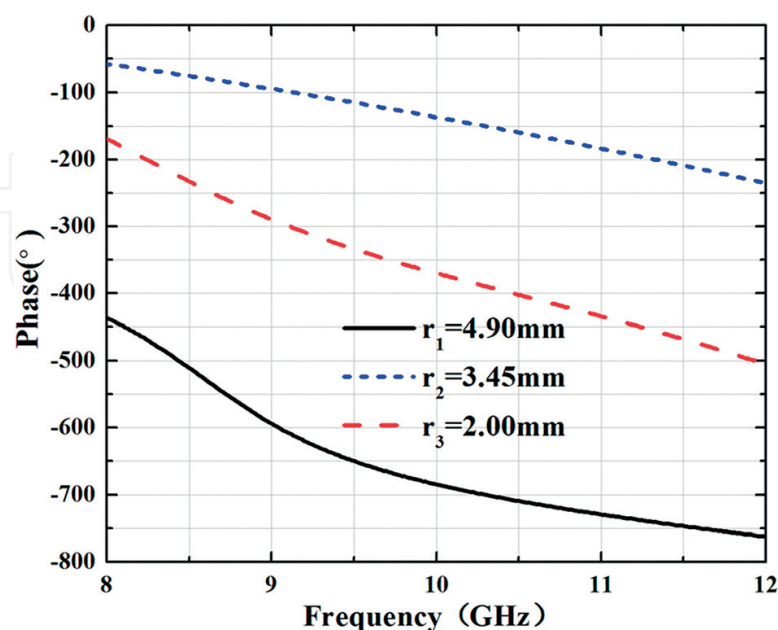


**Figure 6.** Phase of  $S_{11}$  for the CCR unit cell.

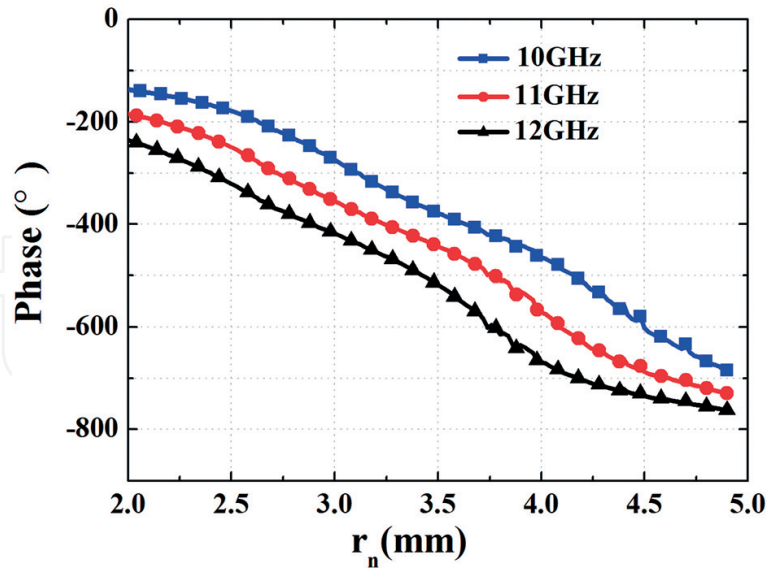


Figure 7. Reflected phase change with  $r_n$  at (a) 10 GHz, (b) 11 GHz, and (c) 12 GHz.

$y = n \times p$  ( $n = 0, \pm 1, \pm 2, \pm 3 \dots$ ). In order to control the phase of the reflected wave well, the maximum phase difference along the  $+x$  direction should be over  $360^\circ$ . However, taking the fabrication cost into consideration, the area of the MS should be not very large. From the unit cell design, we find that the CCR unit cell has a broadband character during 10–12 GHz. At the frequency of 10 GHz, we set  $L = 40$  mm and seven unit cells are used in  $+x$  direction to achieve about  $385^\circ$  phase difference comparing with the first unit cell. Considering that the phase distribution on the MS should be symmetry, we use  $13 \times 13$  unit cells to satisfy the whole profile in  $xoy$ -plane, and the two-dimensional phase distribution of the MS is shown

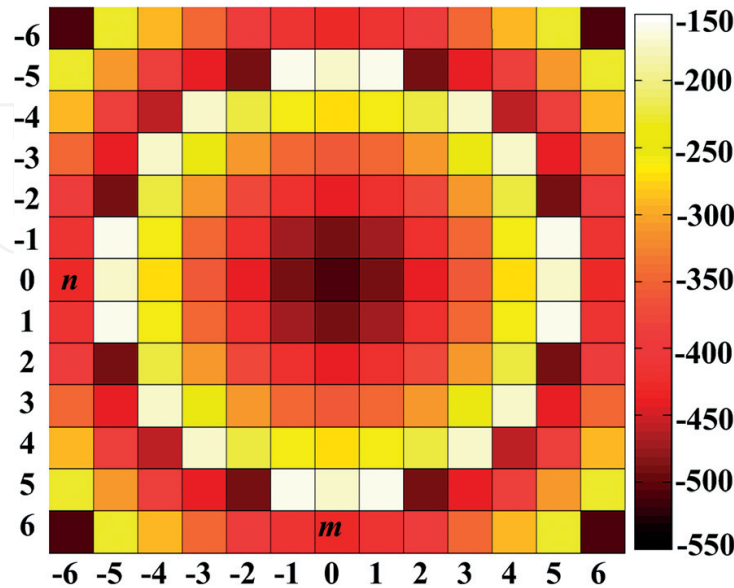
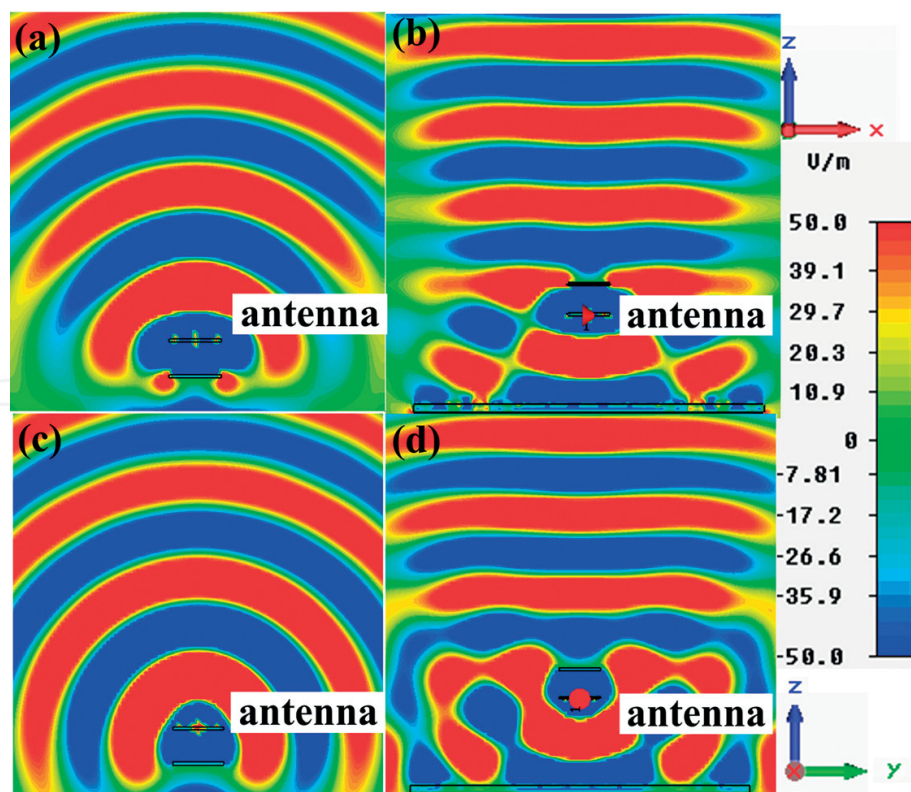


Figure 8. Absolute phase distribution on the focusing MS.

in **Figure 8**. The reflected phase of CCR unit cell has a range of  $[-684^\circ, -136^\circ]$  at 10 GHz, we choose the middle range of the reflected phase  $[-510^\circ, -150^\circ]$  which has better broadband character to design the focusing MS. The parameter  $r_n$  varies from 4.2 to 2.2 mm in this design, and when the phase difference between one unit cell and the first unit cell (reflected phase is  $-510^\circ$ ) is over  $360^\circ$  the reflected phase of this location should be deducted by  $360^\circ$ . In order to illuminate the MS, we choose a spiral antenna as the feed source, and a metal ground is added at the bottom to make the antenna radiate only to the MS. The electric field distributions of the spiral antenna without and with the MS at 10 GHz are shown in **Figure 9**. As shown, both in the two orthogonal planes, MS transforms the quasi-sphere wave emitted by the spiral antenna to plane wave as the theoretical prediction, and it is the mechanism of the proposed high-gain antenna. The simulated and measured voltage standing wave ratios (VSWR) are shown in **Figure 10**. It is shown that the impedance band of the antenna covers the operating band (10–12 GHz) of the MS well.

Then, the 3D radiation patterns at 10, 11, and 12 GHz are shown in **Figure 11**, it can be concluded from the figures that the gain of the feed source is remarkably enhanced and pencil-shaped radiation patterns are achieved. To clearly depict the antenna gain-enhancement via reflected MS, the 2D radiation patterns of the antenna with/without the MS are shown in **Figure 12**. As shown, the antenna beam width has been decreased greatly and the peak gain has been enhanced greatly compared with the planar spiral antenna. It is also necessary to notice that the source is right circular polarization, while the MS antenna is left circular



**Figure 9.** Simulated electric field distribution in (a, b)  $xoz$ -plane and (c, d)  $yo$  $z$ -plane for the spiral antenna (a, c) without the MS and (b, d) with the MS.

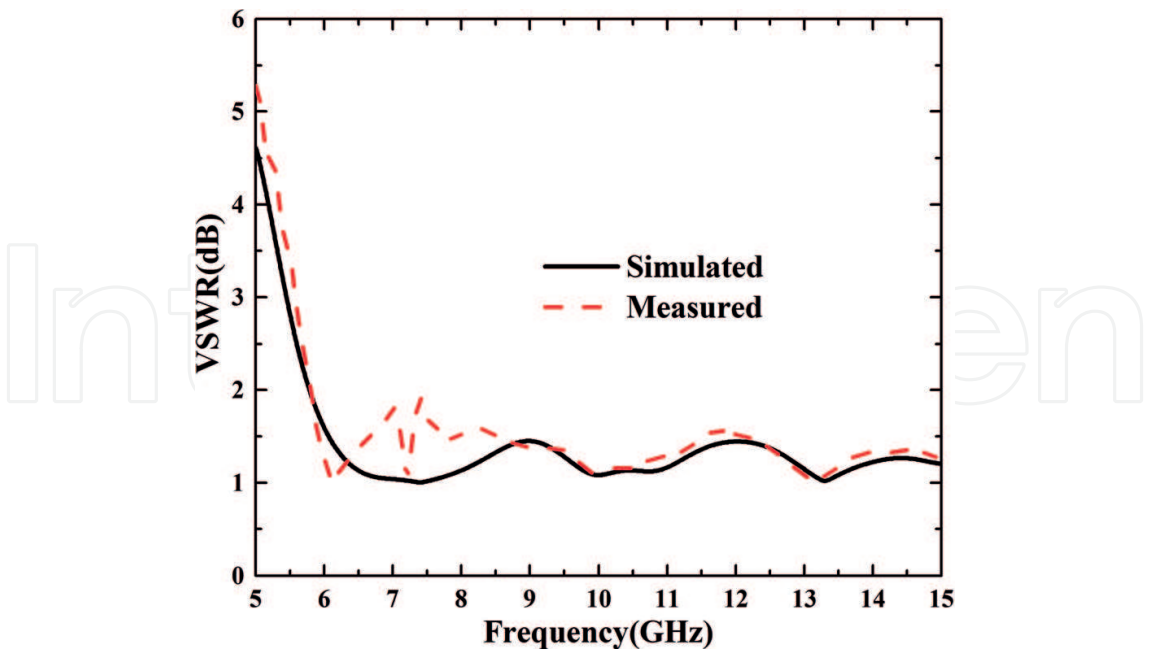


Figure 10. Simulated and measured VSWR of the spiral antenna.

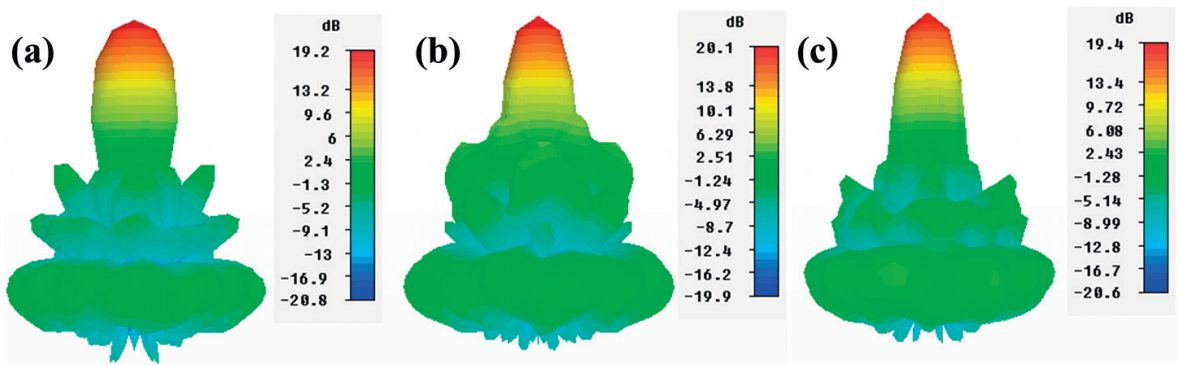


Figure 11. 3D simulated farfield radiation pattern for (a) 10 GHz, (b) 11 GHz, and (c) 12 GHz.

polarization, and the cross-polarization component of the source antenna is also enhanced by the MS while it is still much lower than the copolarization at the main radiation direction.

At last, the proposed MS antenna has been fabricated and assembled, and the photographs are shown in **Figure 13**. The farfield results of the novel MS antenna are measured in an anechoic chamber. **Figure 14** shows the simulated and measured peak realized gain in the band of 8–13 GHz. As shown, the  $-1$  dB gain bandwidth of the proposed antenna is 10–12.3 GHz (with the fractional bandwidth is 20.6%), and in this band, the peak gain has an enhancement of 13.5 dB comparing with the spiral antenna in average. The peak gains at the frequencies of 10, 11 and 12 GHz are 19.2, 20.1 and 19.4 dB, respectively. Then, the aperture efficiency (AE) can be calculated by Eq. (4), where  $\lambda_0$  is the free space wavelength and  $D$  is the side length of the MS. The calculated efficiencies at 10, 11 and 12 GHz are 35.2,



35.8, and 25.6%, respectively. And **Figure 15** shows that the 3 dB axial ratio bandwidth covers the band of 10–12 GHz approximately.

$$AE = \text{Gain} \times \frac{\lambda_0^2}{4\pi D^2} \quad (4)$$

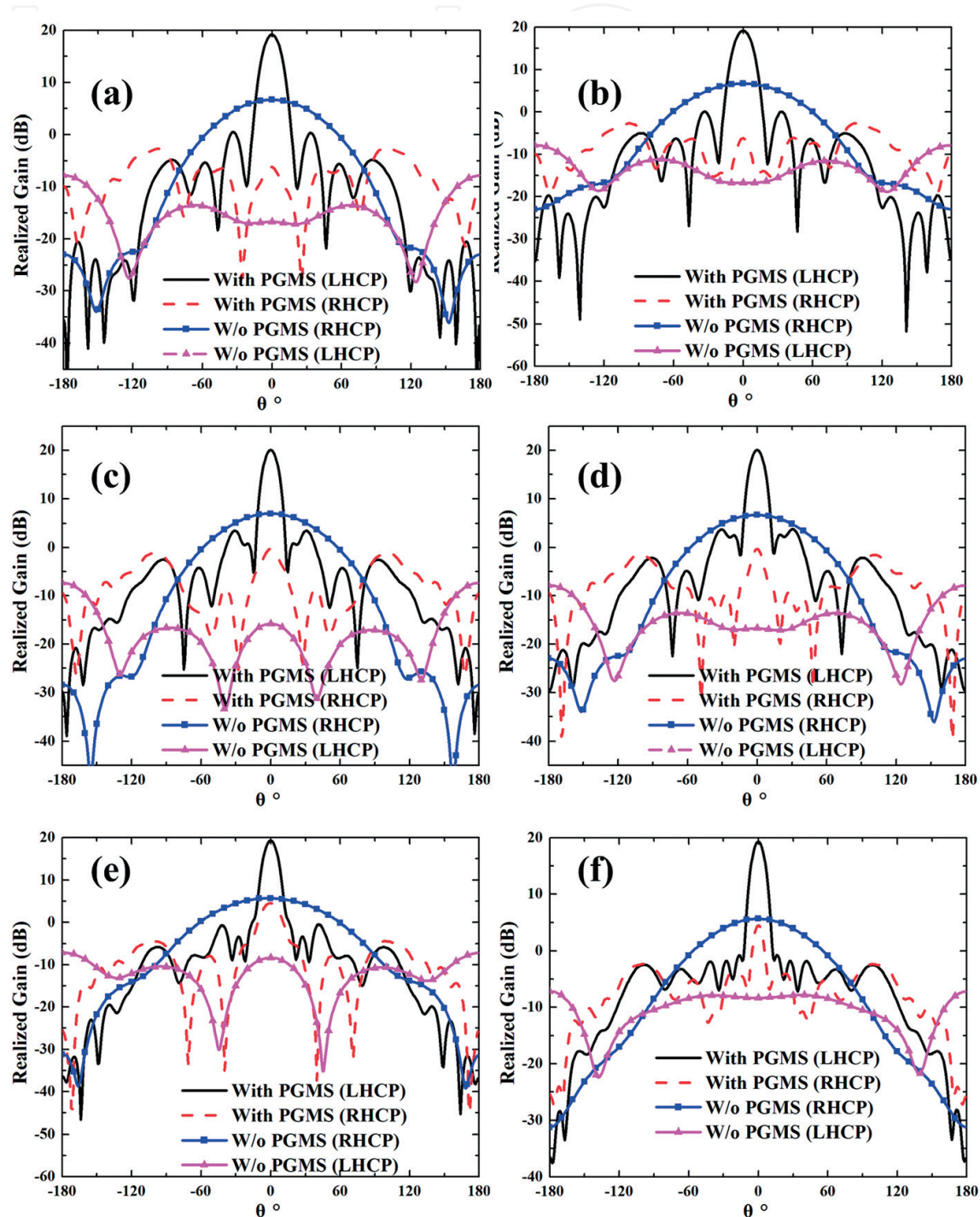


**Figure 12.** Simulated farfield radiation patterns at (a, b) 10 GHz, (c, d) 11 GHz, and (e, f) 12 GHz of the spiral antenna with and without the MS in (a, c, e) *xoy*-plane and (b, d, f) *yo**z*-plane.

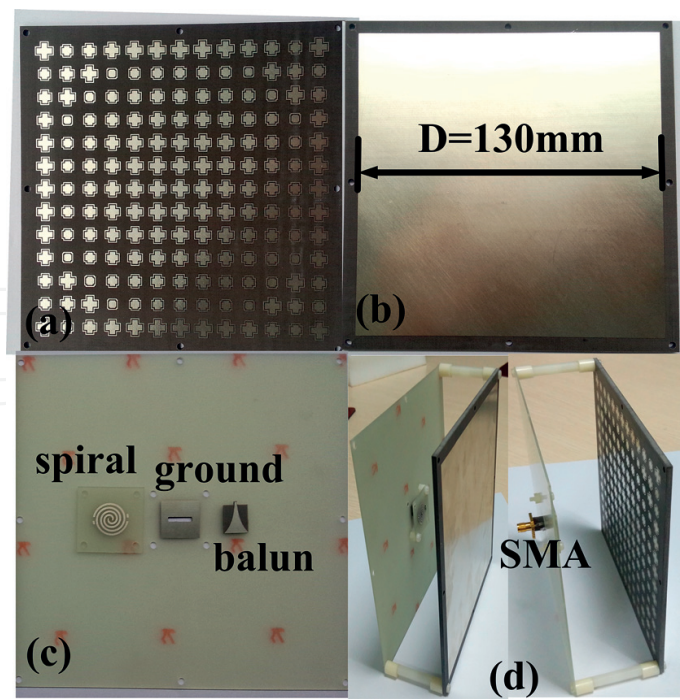


**Figure 13.** The photographs of the MS antenna. (a) Top view, (b) bottom view of the reflected MS, (c) components of the spiral antenna, and (d) free view of the MS antenna.

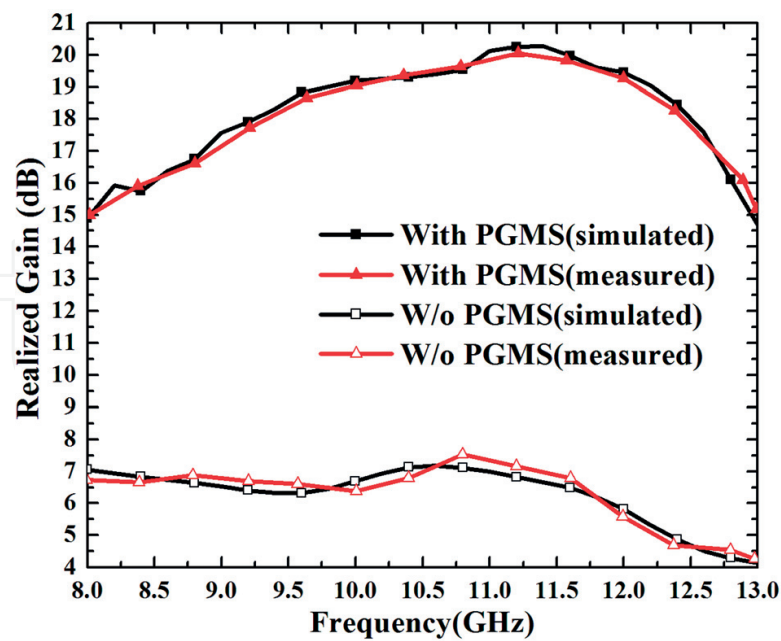


**Figure 14.** Measured and simulated peak gain of the spiral antenna with/without the focusing MS.



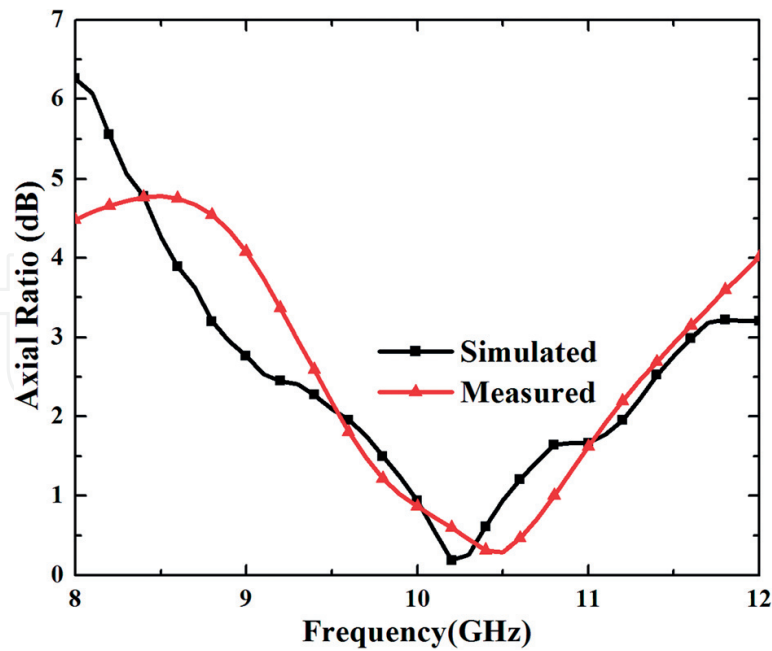


Figure 15. Measured and simulated axial ratio of the MS antenna.

## 2. Wideband multifunctional metasurface for polarization conversion and gain enhancement

The polarization state is one of the most important characteristics of the EM waves. We can classify the polarization conversion MS (PCMS) [14–19] into two categories according to the format of the MS—transmitting type [14–17] and reflecting type [18, 19]. Also, the PCMS also can be classified into cross-polarization conversion one [14–16, 18] or linear-to-circular/circular-to-linear (LTC/CTL) one [17, 19] according to specific functionalities. However, the mentioned PCMSs are all illuminated by plane waves and the radiation performances will be more or less deteriorated when they are directly feed by a spherical feed source like Vivaldi antenna. Taking the overall performances into consideration, a technique should be adopted for a PCMS design to control the direction of the scattering wave for spherical wave excitation. The focusing MS mentioned above can transfer the incident plane wave to its focal point, and vice versa. So, it can be predicted that the combination of the PCMS with focusing MS will improve the radiation performance of the system.

### 2.1. Linear-to-circular metasurface design

Anisotropic MSs have the character of manipulating electromagnetic waves with different polarizations, respectively. We still adopt the CCR unit cell shown in Figure 16 to design an anisotropic MS. Compared with the unit cell shown Figure 1, we set  $r_x$  and  $r_y$  with different values to

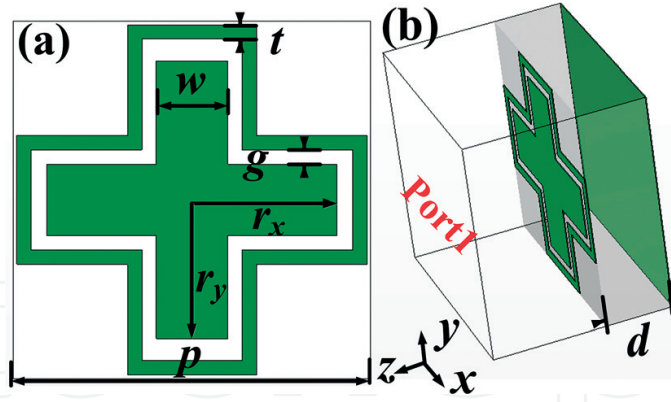


**Figure 16.** Topology of the proposed LTC-PCMS unit cell with  $g = t = 0.4$  mm,  $p = 10$  mm, and  $d = 3$  mm. (a) Front view and (b) perspective view. The metallic is shown in green, while the slot is shown in white.

make the reflecting phase change with the polarization of the incident wave. The reflection matrix ( $R$  matrix), which connects the incident fields and reflected fields, can be described as:

$$R = \begin{pmatrix} R_{xx} & R_{yx} \\ R_{xy} & R_{yy} \end{pmatrix} \quad (5)$$

where  $R_{ij}$  represents the reflection coefficient of  $j$  polarization incident wave and  $i$  polarization reflected wave. And we use  $\text{Am}(R_{ij})$  and  $\text{Arg}(R_{ij})$  to describe the amplitude and phase of  $R_{ij}$ , respectively. At the case of  $r_x = 4.06$  mm and  $r_y = 3.6$  mm, we can obtain that  $\text{Am}(R_{xx}) = \text{Am}(R_{yy}) = 1$ ,  $\text{Am}(R_{yx}) = \text{Am}(R_{xy}) = 0$  and  $\text{Arg}(R_{xx}) - \text{Arg}(R_{yy}) \approx -90^\circ$  around 10 GHz from **Figure 17**. In this situation, the  $R$  matrix is,

$$R = \begin{pmatrix} -j & 0 \\ 0 & 1 \end{pmatrix} e^{-j\varphi} \quad (6)$$

We suppose that the LTC-PCMS is illuminated by a plane wave propagating along  $-z$  direction, then the formulation of the incident wave can be described as Eqs. (7) and (8).

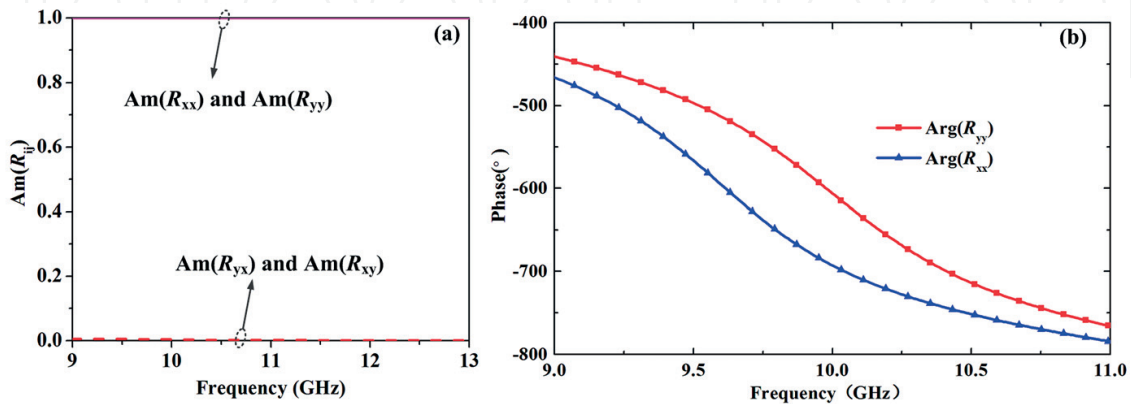


**Figure 17.** The (a) amplitudes and (b) angles of the  $R$  matrix.

$$\vec{E}_i = (\hat{x}E_x + \hat{y}E_y)e^{-jkz} \quad (7)$$

$$\begin{pmatrix} E_x \\ E_y \end{pmatrix} = \begin{pmatrix} \cos \theta \\ \sin \theta \end{pmatrix} e^{-jkz} \quad (8)$$

where  $k$  is the wave number. In the following, we will discuss that our LTC-PCMS supports linear wave to LHCP or RHCP wave conversion in two special cases.

For the case of  $\theta = 45^\circ$ , the incident E fields can be described as:

$$\begin{pmatrix} E_x \\ E_y \end{pmatrix} = \frac{\sqrt{2}}{2} \begin{pmatrix} 1 \\ 1 \end{pmatrix} e^{-jkz} \quad (9)$$

Then, the reflected E fields can be calculated as:

$$\begin{aligned} \begin{pmatrix} E_{rx} \\ E_{ry} \end{pmatrix} &= R \frac{\sqrt{2}}{2} \begin{pmatrix} 1 \\ 1 \end{pmatrix} e^{jkz} e^{-j\varphi} \\ &= \frac{\sqrt{2}}{2} \begin{pmatrix} -j \\ 1 \end{pmatrix} e^{jkz} e^{-j\varphi} \end{aligned} \quad (10)$$

$$\begin{aligned} \vec{E}_r &= E_{rx}\hat{x} + E_{ry}\hat{y} \\ &= \frac{\sqrt{2}}{2} (-j\hat{x} + \hat{y}) e^{jkz} e^{-j\varphi} \end{aligned} \quad (11)$$

As described in Eq. (11), it can be concluded that the polarization of the reflected wave is LHCP. In the second case of  $\theta = 135^\circ$ , we can obtain following results by taking similar calculations.

$$\begin{aligned} \vec{E}_r &= E_{rx}\hat{x} + E_{ry}\hat{y} \\ &= \frac{\sqrt{2}}{2} (j\hat{x} + \hat{y}) e^{jkz} e^{-j\varphi} \end{aligned} \quad (12)$$

In this situation, a RHCP reflected wave has been obtained. **Figure 18** depicts a practical realized scheme of our system, where the LTC-PCMS fed by a Vivaldi antenna is built by  $13 \times 13$  single-layered CCR unit cells. The voltage standing wave ratio (VSWR) with its geometrical parameters has been shown in **Figure 19**. We can conclude that the Vivaldi antenna has a VSWR less than 2 dB within the frequency band of 9–15 GHz. Three-dimensional radiation patterns and AR results of the LTC-PCMS are shown in **Figure 20**. As shown, the far-field patterns achieve CP radiation but the directivity of the Vivaldi antenna has been broken by the MS. To conquer this problem, an additional focusing profile needed to be brought in to correct the wave-front of the outgoing wave.

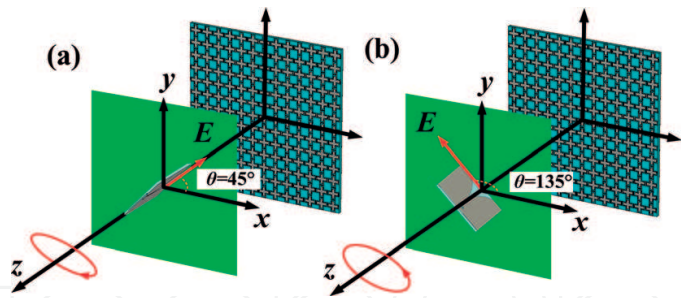


Figure 18. The scheme of proposed two situations for different E field directions at (a)  $\theta = 45^\circ$  and (b)  $\theta = 135^\circ$ .

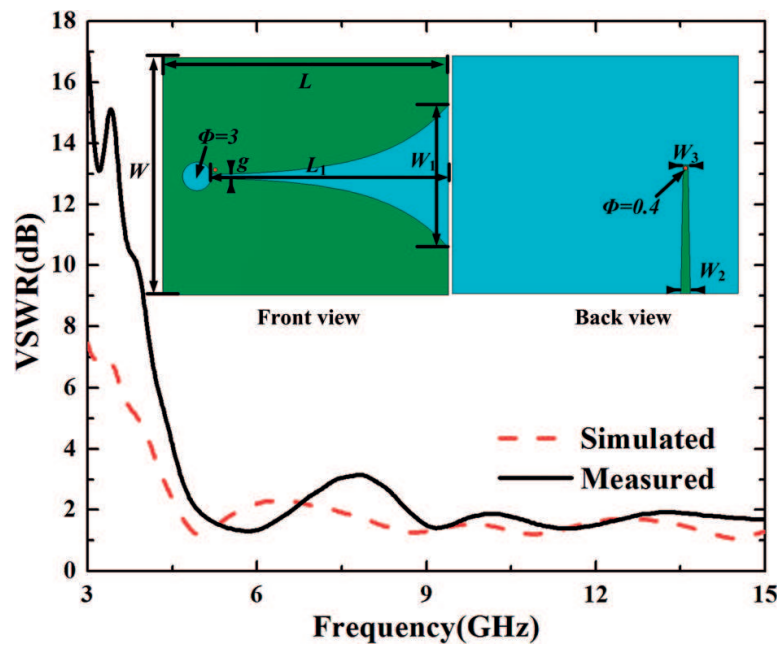


Figure 19. The VSWR of the Vivaldi antenna. The geometrical parameters are  $W = 25$  mm,  $L = 30$  mm,  $L_1 = 25$  mm,  $W_1 = 15$  mm,  $W_2 = 1$  mm,  $W_3 = 0.5$  mm, and  $g = 0.5$  mm.

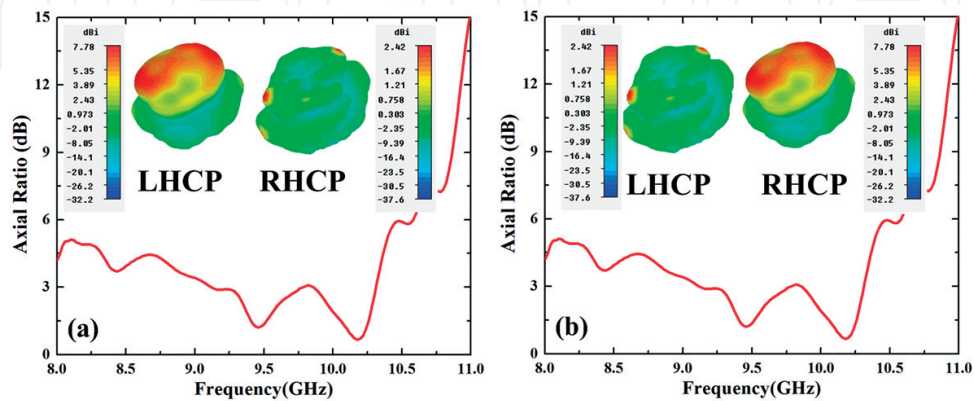


Figure 20. 3D radiation patterns and AR results of the LTC-PCMS for (a)  $\theta = 45^\circ$  and (b)  $\theta = 135^\circ$ .

## 2.2. Multifunctional metasurface design

To ease the design, we want the unit cell can manipulate the  $x$ - and  $y$ -polarized waves independently and completely. By simulations, we find that the single-layered CCR element features good polarization-independence but lacks sufficient phase-tuning range. Then, we propose a bi-layered CCR element to enlarge the phase-tuning range. The phases of  $R_{xx}$  and  $R_{yy}$  of the bi-layered unit cell are shown in **Figure 21**. As shown, the parameter  $r_x$  ( $r_y = 4.06$  mm) just affects the value of  $\text{Arg}(R_{xx})$ , while  $\text{Arg}(R_{yy})$  is almost constant when  $r_x$  increases from 2.3 to 4.06 mm. Meanwhile, the phase range of  $\text{Arg}(R_{xx})$  has reached  $360^\circ$ . Since the CCR unit cell exhibits rotational symmetry, similar conclusion can be obtained by just tuning  $r_y$ . In a word, the phases of  $x$  and  $y$  polarization incident waves are controlled by  $r_x$  and  $r_y$ , respectively, and they do not influence each other. This character will greatly simplify the design of the multifunctional MS.

For focusing MS, the phase difference distribution on the MS has to satisfy Eq. (13).

$$\Delta\varphi(m,n) = \frac{2\pi}{\lambda} (\sqrt{(mp)^2 + (np)^2 + L^2} - L) \pm 2k\pi \quad (k=0,1,2,\dots) \quad (13)$$

where  $L$  is the focal distance,  $m(n)$  is the number of the unit cell in  $x(y)$  direction, and is the phase difference according to the unit cell, which is placed at the origin point ( $m=0, n=0$ ). For LTC-MS, the phase of  $R_{xx}$  must have a  $90^\circ$  difference with the phase of  $R_{yy}$  through each unit cell around 10 GHz.  $\text{Arg}(R_{xx})_{mn}$  is controlled by the parameter of  $r_x$ , while  $\text{Arg}(R_{yy})_{mn}$  is controlled by the parameter of  $r_y$ . For  $x$ -polarization incidence, the phase distribution can be calculated by,

$$\begin{aligned} \text{Arg}(R_{xx})_{mn} - \text{Arg}(R_{xx})_{00} &= \frac{2\pi}{\lambda} (\sqrt{(mp)^2 + (np)^2 + L^2} - L) \pm 2k\pi \\ &= \Delta\varphi_{xx}(m,n) \quad (k=0,1,2,\dots) \end{aligned} \quad (14)$$

While for  $y$ -polarization incidence, the phase distribution is:

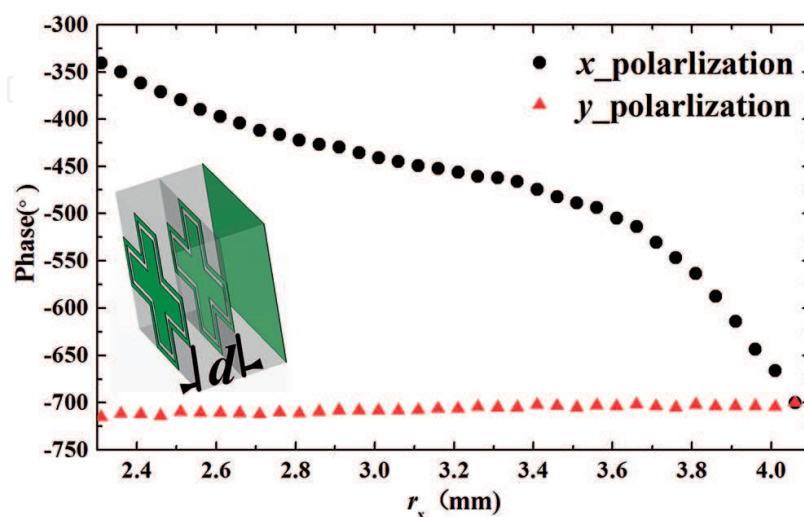


**Figure 21.** Phases of S11 for  $x/y$  polarizations of the dual-layered CCR unit cell with its structure.



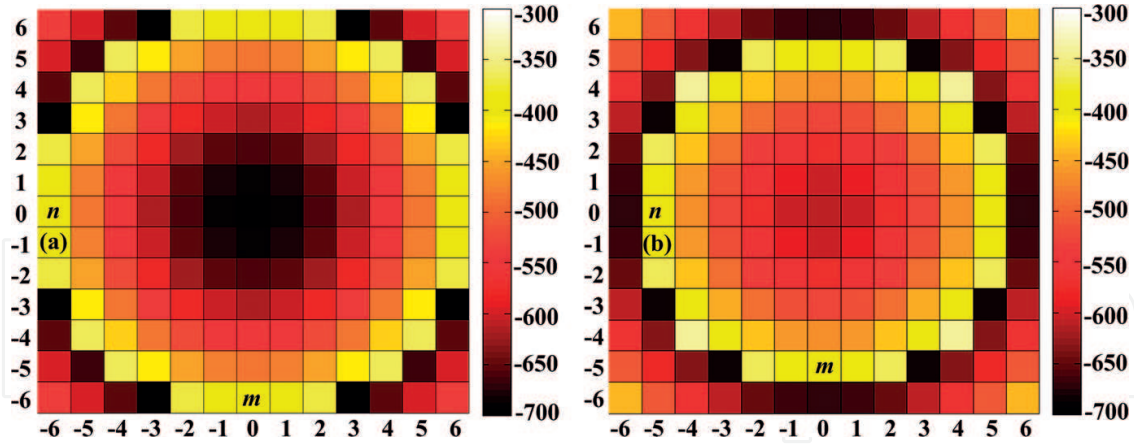


Figure 22. Absolute phase distributions for (a)  $x$  polarization and (b)  $y$  polarization.

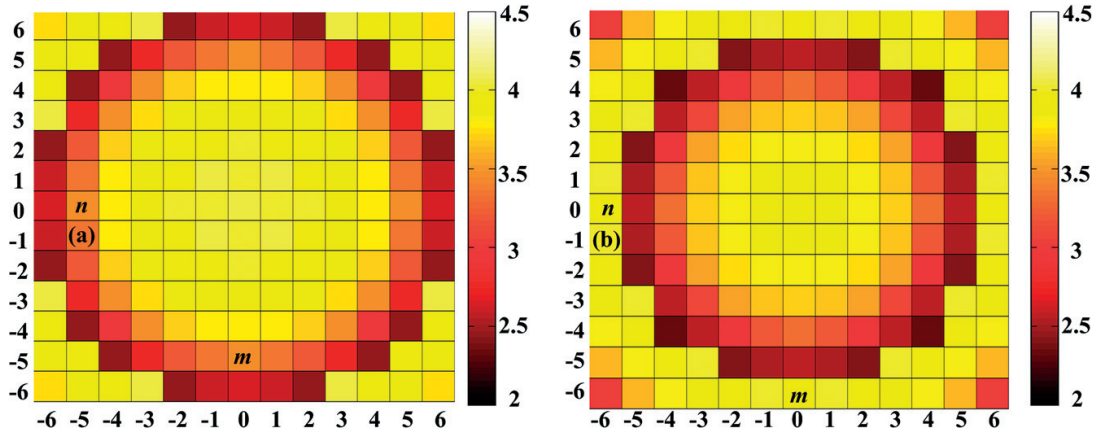


Figure 23. Distributions of (a)  $r_x$  and (b)  $r_y$  on the multifunctional MS.

$$\begin{aligned} \text{Arg}(R_{yy})_{mn} - \text{Arg}(R_{yy})_{00} &= \frac{2\pi}{\lambda} (\sqrt{(mp)^2 + (np)^2 + L^2} - L) \pm 2k\pi \\ &= \Delta\phi_{yy}(m, n) \quad (k=0, 1, 2, \dots) \end{aligned} \quad (15)$$

where, in the focusing LTC-PCMS design, following equations have to be satisfied:  $\text{Arg}(R_{xx})_{00} - \text{Arg}(R_{yy})_{00} = -90^\circ$ . We insert  $L = 2\lambda$ ,  $p = 10$  mm,  $\lambda = 30$  mm, and  $\text{Arg}(R_{xx})_{00} = -700^\circ$  into Eqs. (13) and (14) to obtain the phase distributions shown in **Figure 22**. And then the values of  $r_x$  and  $r_y$  at each position ( $m, n$ ) on the MS can be ascertained and shown in **Figure 23**.

### 2.3. Circular-polarized antenna design

Then, the proposed MS model is built in CST based on the matrixes of  $r_x$  and  $r_y$ , and a Vivaldi antenna is placed 60 mm away from MS as a feed source. As shown in **Figure 18(a)**, we first set  $\theta = 45^\circ$  and an LHCP-reflected wave will be obtained consequently. **Figure 24** describes the near-field electric field distributions in  $xoz$ - and  $yoz$ -planes, which illustrates that the incident plane wave has been converted into near-plane wave. For farfield results, the 2D patterns of  $xoz$ - and  $yoz$ -planes are shown in **Figure 25** and the pencil-shaped 3D radiation pattern and the

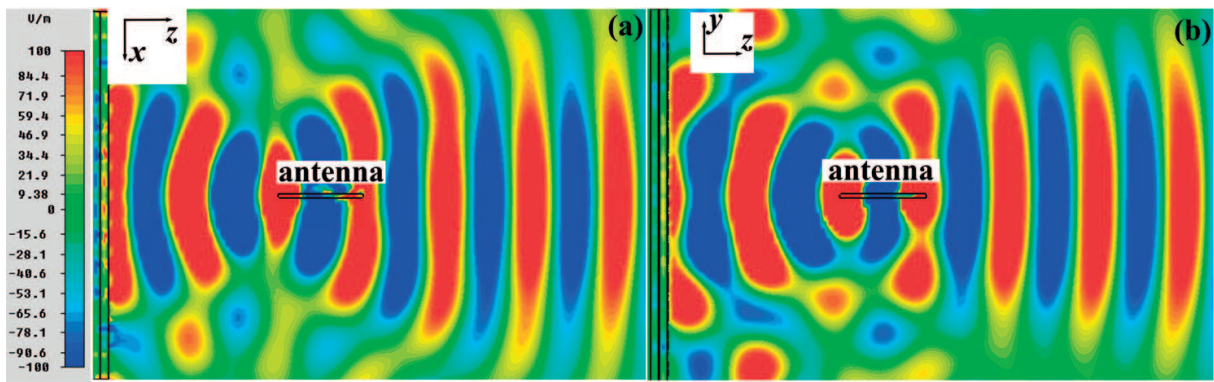


Figure 24. Electric field distributions in (a) xoz and (b) yoz plane at 10 GHz.

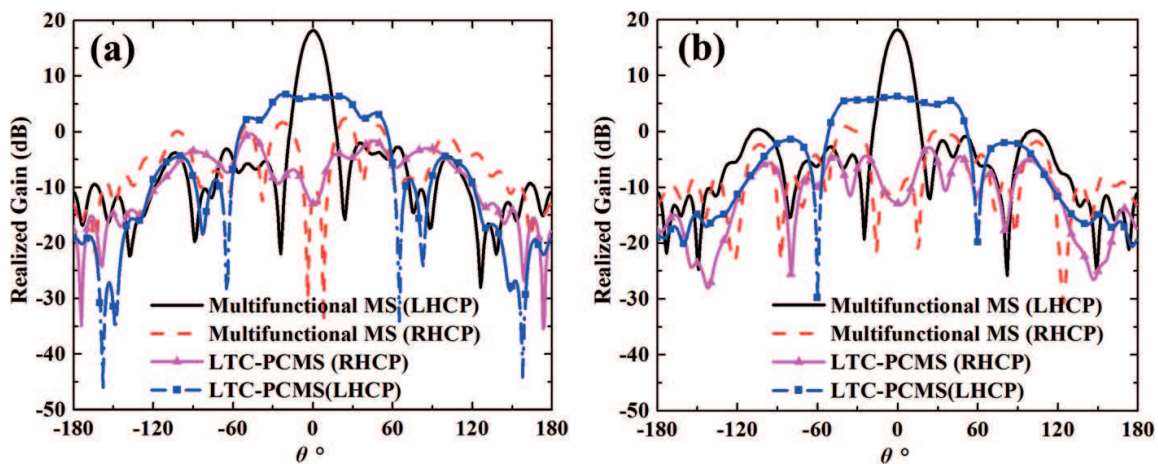


Figure 25. 2D radiation patterns at 10 GHz (a) xoy-plane (b) yoz-plane.

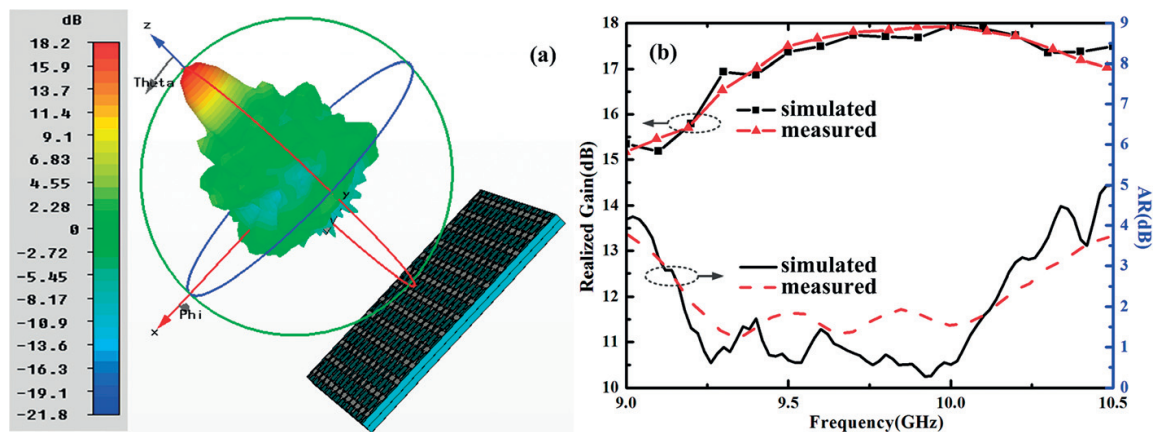


Figure 26. (a) 3D radiation pattern (b) simulated and measured results of axis ratios and realized gains.

realized gains with AR results are shown in **Figure 26**. Comparing with LTC-PCMS, the new multifunctional MS enhances the gain and decreases beam width of the antenna in 3 dB AR band of 9.12–10.2 GHz. Specially, the realized gain has been enhanced 12 dB and a half power beam width of  $13^\circ$  has been achieved at 10 GHz.



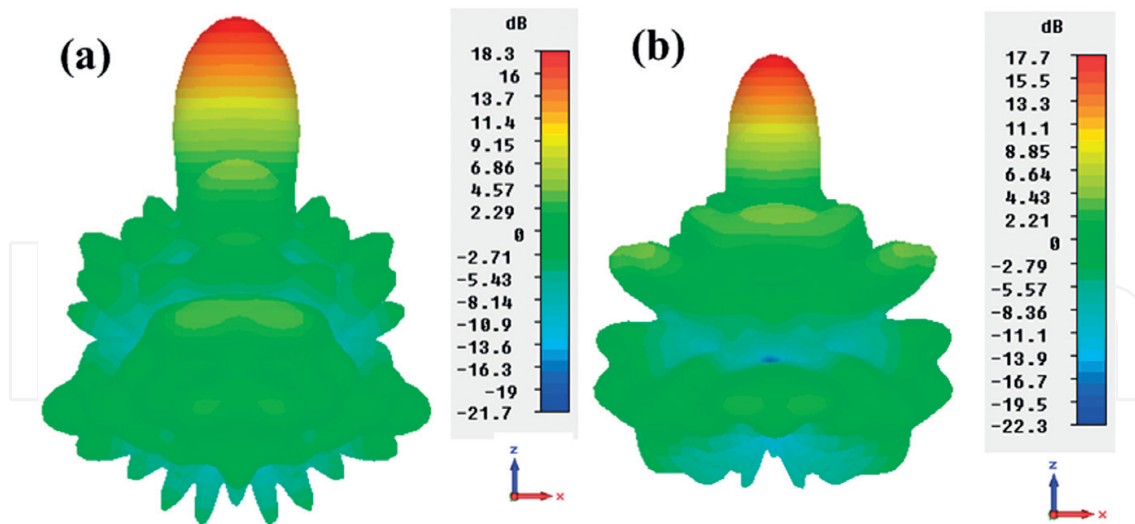


Figure 27. 3D radiation patterns for (a)  $\theta = 0^\circ$  and (b)  $\theta = 90^\circ$ .

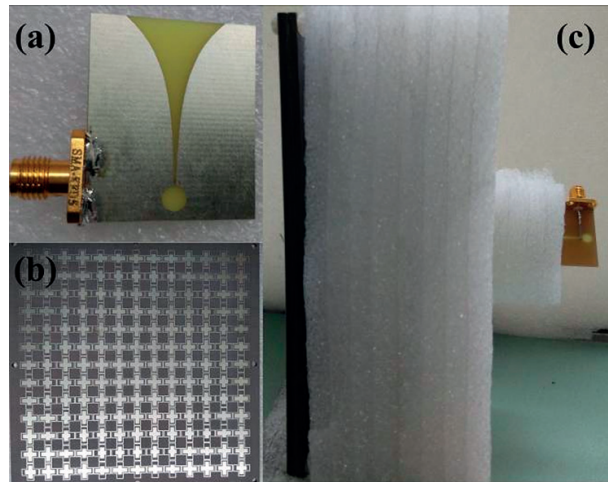


Figure 28. Photographs of the fabricated sample. (a) Vivaldi antenna, (b) multifunctional MS, and (c) whole system.

In addition, we simulate the models of  $\theta = 0^\circ$ ,  $90^\circ$ , and  $135^\circ$ . It is similar as the LTC-PCMS, the results for  $\theta = 135^\circ$  and  $45^\circ$  are the same expect that the copolarization is LHCP for  $\theta = 45^\circ$ , while it is RHCP for  $\theta = 135^\circ$ . For  $\theta = 0^\circ$ ,  $x$ -polarization reflecting wave is obtained as shown in **Figure 27(a)**. While for  $\theta = 90^\circ$ , and  $y$ -polarization reflecting wave is obtained as shown in **Figure 27(b)**. To some extent, the whole system is polarization-reconfigurable to some extent. Finally, the photographs of the fabricated sample are shown **Figure 28**.

### 3. High-gain lens antenna based on multilayer metasurface

Compared with the reflected MS, the feed of the transmitted MS does not block the radiated wave, making it more suitable for a high-gain antenna design. However, the design of the transmitting MS is more difficult since the transmitting efficiency must be taken into consideration.

In this section, we proposed a four-layered transmitting MS with a parabolic phase profile at 10 GHz. The MS elements are cautiously designed and optimized, aiming at affording high transmitting efficiencies for all the building elements. In that case, the MS can focus the incident plane wave with high efficiency. In current design, a patch antenna operating at 10 GHz is placed at the focal point of the MS to feed the PGMS and the F/D is designed as 0.19. The quasi-spherical wave emitted by the source will be transformed to near-plane wave by the MS, and thus a high gain lens antenna with pencil-shaped beam will be achieved.

### 3.1. Multilayer metasurface unit cell design

The structure of the unit cell, as shown in **Figure 29**, consists of a four metal layers and a three dielectric layers. The metal layer consists of a circular patch and a square outer frame. The transmission phase changes with the radius of  $r_n$  of the circular patch. The dielectric substrate has a relative dielectric constant of 2.65 and a thickness of  $d = 1.5$  mm, of which  $t = 0.1$  mm,  $p = 10$  mm. We simulate the elements with one, two, and three layers, respectively, in CST Microwave Studio, and their simulation results, the curves of phase, and amplitude varying with the frequency, are shown in **Figure 30**. It can be seen from the figure that when the patch size of the three units is changed, the transmission coefficients at 10 GHz are all above 0.8, and the phase control range increases with the increase of the number of layer. The phase coverage of the unit cell contains three dielectric layers already exceeding  $360^\circ$ . The curves of transmitted phase and amplitude varying with the patch size are shown in **Figure 31**.

### 3.2. High-efficiency transmitted focusing metasurface design

For designing the transmitted focusing MS, the phase distribution should also obey Eq. (3). To not lose generality, we arbitrarily select  $f = \lambda = 30$  mm in this particular design. The phase distribution is shown in **Figure 32**. And we can obtain the parameter distribution shown in **Figure 33** and build the MS model. Owing to the narrow band characteristic of the MS, we adopt a microstrip patch antenna as the feed source, and its structure and reflection coefficient are shown in **Figure 34**. The feed source and the MS were simulated in CST, respectively. The electric-field distributions at  $xoz$ - and  $yo$ z-planes at 10 GHz are shown in **Figure 35**. It can be seen from the figure that the spherical wave emitted by the feed passes through the MS and the transmitted

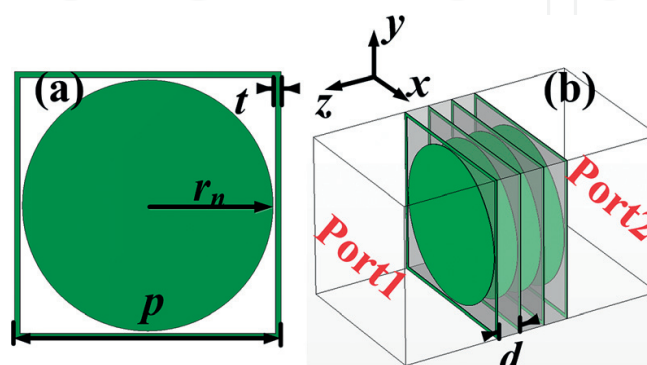


**Figure 29.** Structure of the metasurface unit and the simulated setup. (a) Top view and (b) perspective view.

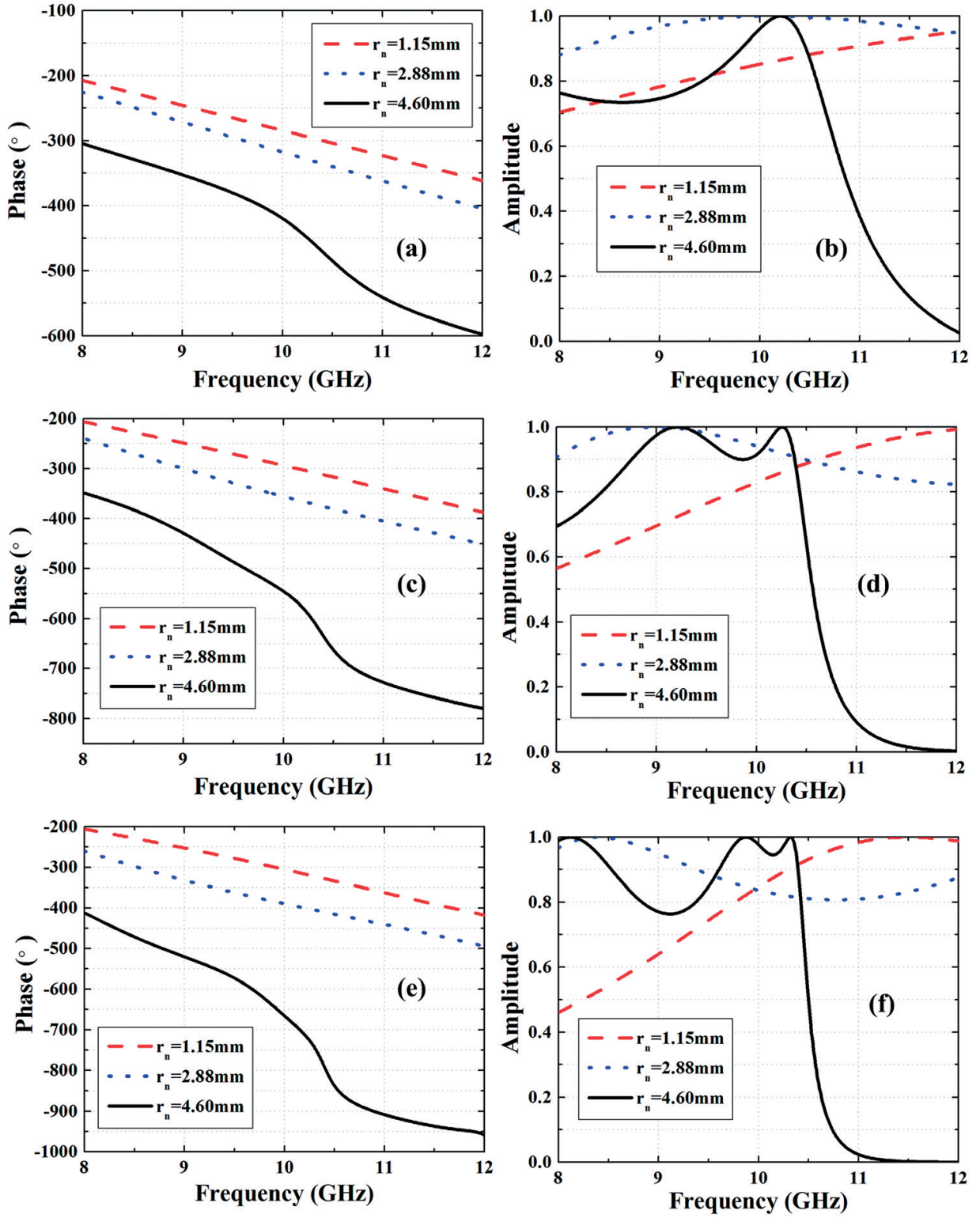
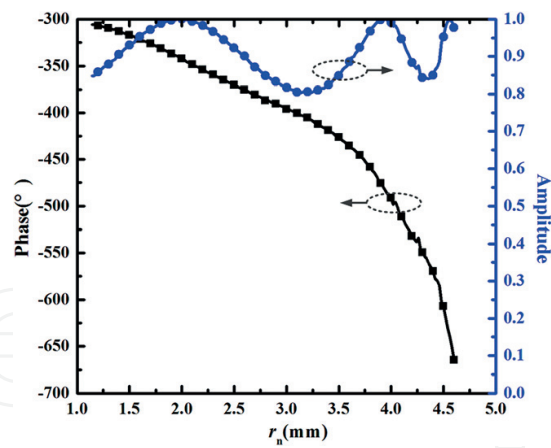
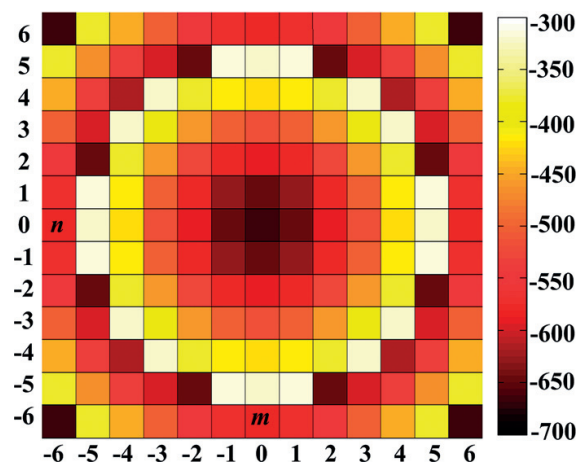


Figure 30. Phase (a, c, e) and amplitude (b, d, f) of S21 for single (a, b), two (c, d), and three (e, f) dielectric layers.

wave becomes a near-plane wave. The result is in agreement with the theoretical prediction, and it also means that the transmitted MS can be used to enhance the gain of the feed antenna. The pen-shaped farfield pattern given in Figure 36 is a more powerful proof of this characteristic.



**Figure 31.** Simulated transmission phase difference (black square dots) and amplitude (blue circle dots) of the unit with different radius  $r_n$  of the solid circle ( $n = 1, 2 \dots 8$ ) at 10 GHz.



**Figure 32.** Absolute phase distribution of the focusing MS.

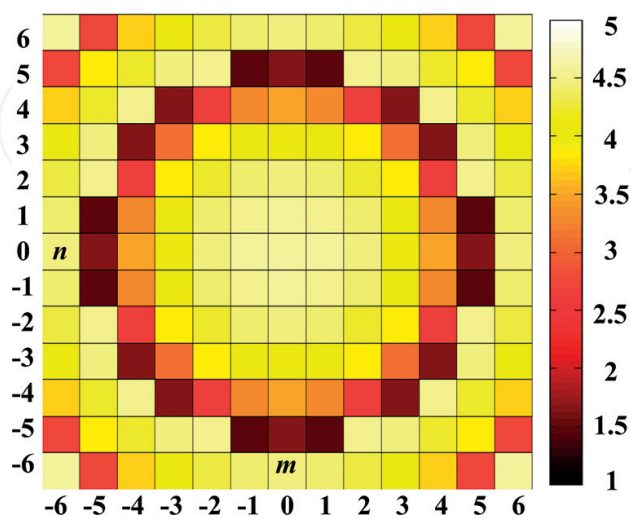


**Figure 33.** The distribution of  $r_n$  on the MS.



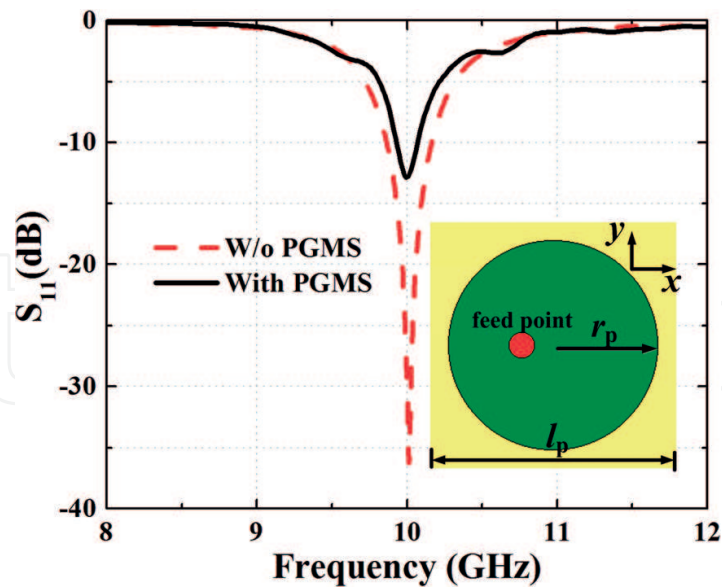


**Figure 34.** The structure of the patch antenna and its measured reflection coefficients with/without the PGMS.  $l_p = 12$  mm and  $r_p = 5.1$  mm.

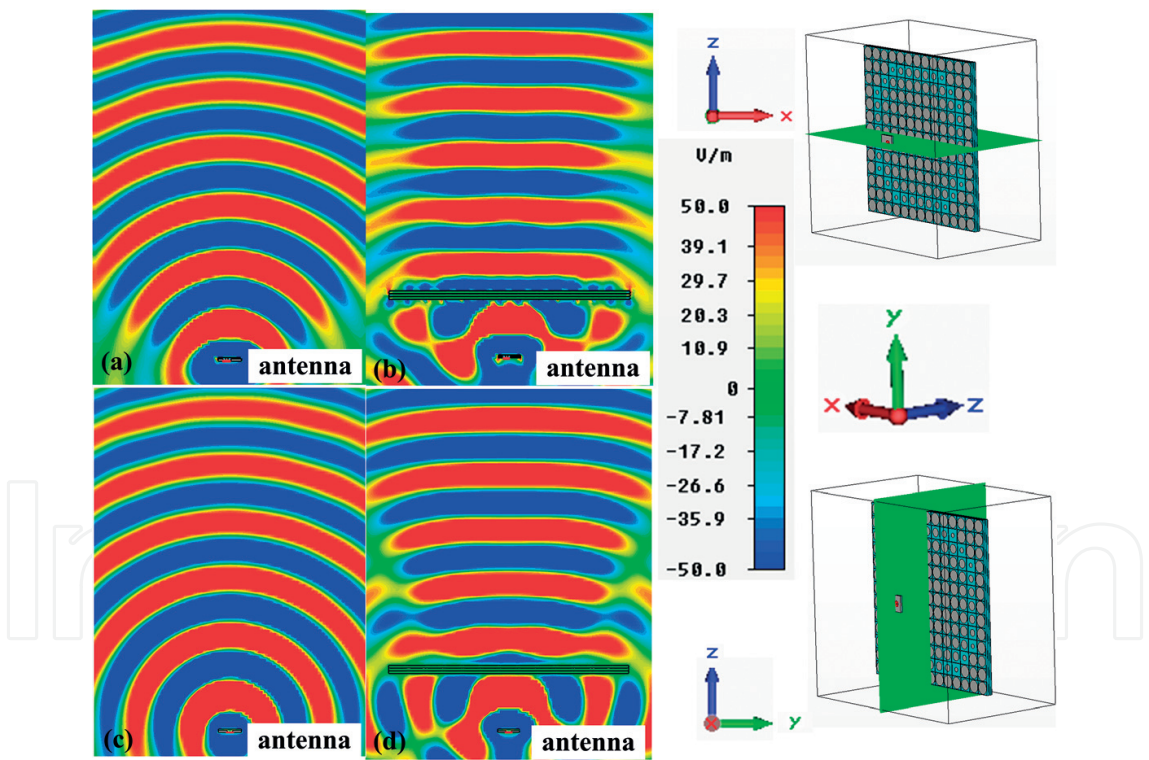


**Figure 35.** Simulated electric field distribution ( $E_x$ ) 10 GHz in (a, b)  $xoz$ -plane and (c, d)  $yo$ z-plane, respectively, for the patch antenna without (a, c) and (b, d) with the metasurface.

**3.3. Lens antenna assembling and measurement**

The multilayer MS is fabricated and then assembled with a patch antenna. The sample photographs are shown in **Figure 37**. We test the MS antenna in the microwave anechoic chamber. **Figure 38** shows the simulated and measured patterns of the  $xoz$ - and  $yo$ z-planes at

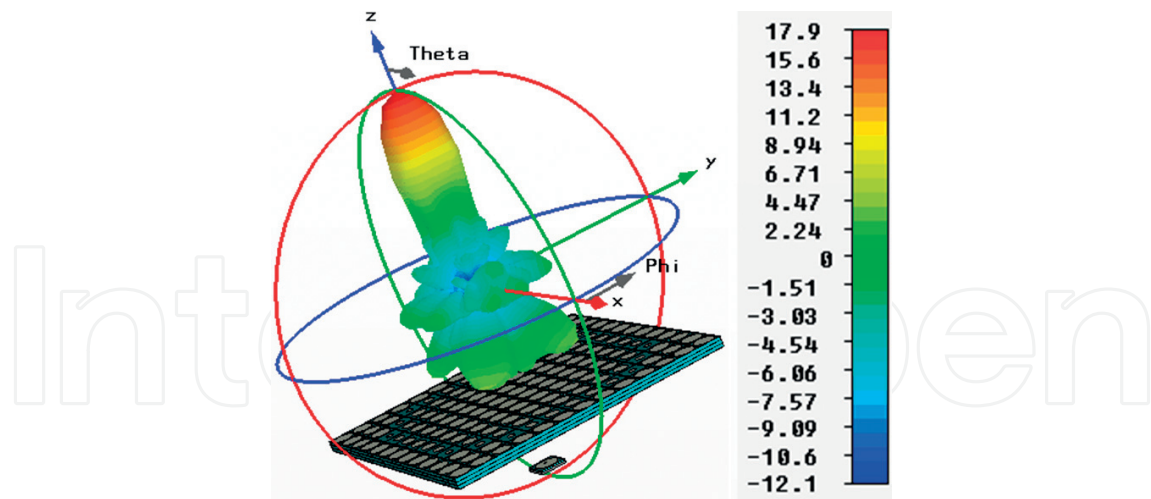


Figure 36. Three-dimensional pen shape pattern at 10 GHz of antenna.

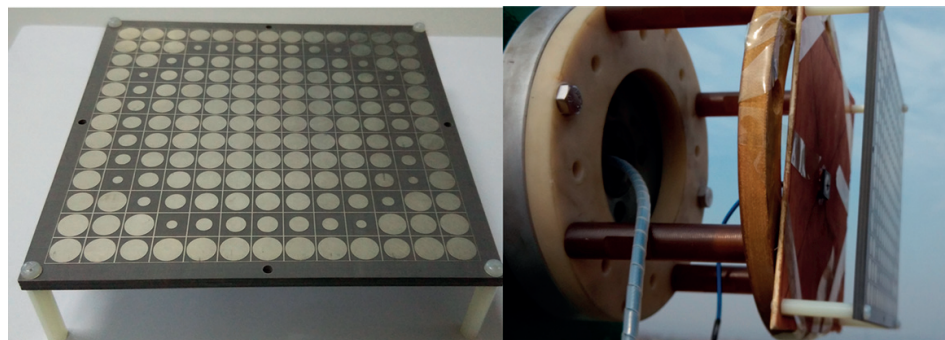


Figure 37. Photographs of high-gain lens antenna.

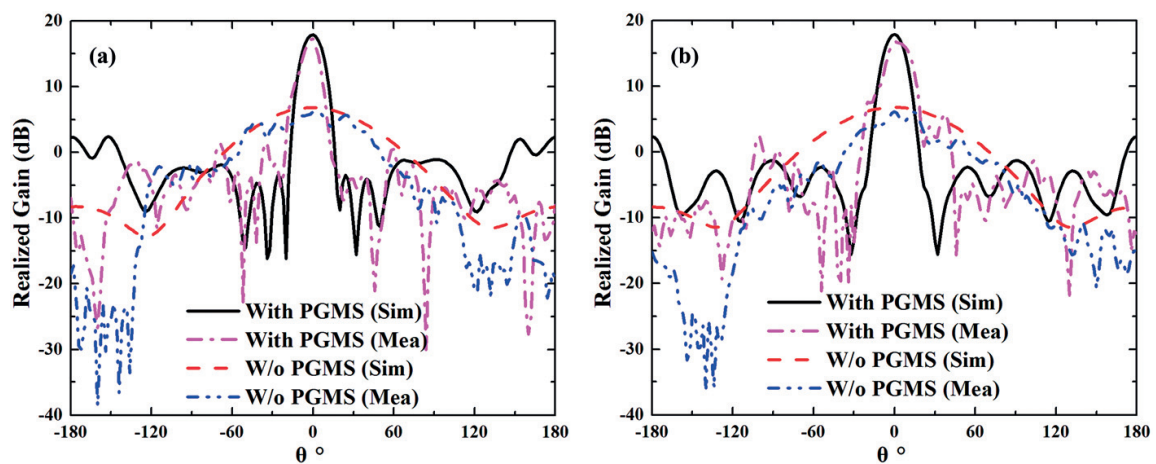


Figure 38. Simulated and measured farfield radiation patterns at 10 GHz of the patch antenna with and without the metasurface. (a) *xoy*-plane and (b) *yoz*-plane.

the 10 GHz of the MS and the contrasted patterns of the bare patch antenna. It can be seen from the figure that the MS increases the gain of the patch antenna and narrows the width of the beam, in which the gain enhancement is 11.6 dB and the half-power beam width decrease

is  $66^\circ$ . The aperture efficiency of antenna at 10 GHz can be calculated to be about 30% by Eq. (4) (Figure 38).

#### 4. Single-layer metasurface for ultrathin planar lens antenna application

As we all known, it is hard to cover  $360^\circ$  phase shift range with satisfying efficiencies by single-layered (bi-layered metal) structures, though they are easier of fabrication. Multilayer stack adopted in above section is a valid technique to expand the phase shift range of MS. However, it is not the only method to achieve this goal. In Ref [20], three kinds of single-layer unit cells are used together to provide adequate phase range by skillfully connecting each phase shift section of them. In this section, an element group consist of two similar single-layered transmitting unit cells was designed. The phase steering ranges of the two elements have been well connected to achieve a phase shift range of  $415^\circ$ . And we use this element group to successfully design an ultrathin planar lens antenna.

##### 4.1. Single-layer element design

The structures of the element 1 and the element 2 are shown in Figure 39, in which the metal layer of the element 1 is a cross and a double cross-ring structure (cross and double cross-ring, CDCR), and the metal layer of the element 2 is a cross and cross-ring structure (cross and cross-ring, CCR). The dielectric layers of the two elements are all 3 mm thick with a relative dielectric constant of 4.3. The dimensions shown in Figure 39 are,  $p = 8$  mm,  $w = 0.9$  mm,  $g = t = 0.15$  mm,  $r_1 = 3.9$  mm, and  $r_2 = 3.7$  mm. Element 1 and element 2 regulate their phases by changing the values of  $r_{1n}$  and  $r_{2n}$  respectively. For the CDCR element structure, the transmission coefficient amplitude curve of  $r_{1n} = 3.38$  mm and  $r_{1n} = 1.10$  mm are shown in Figure 40. In this figure,

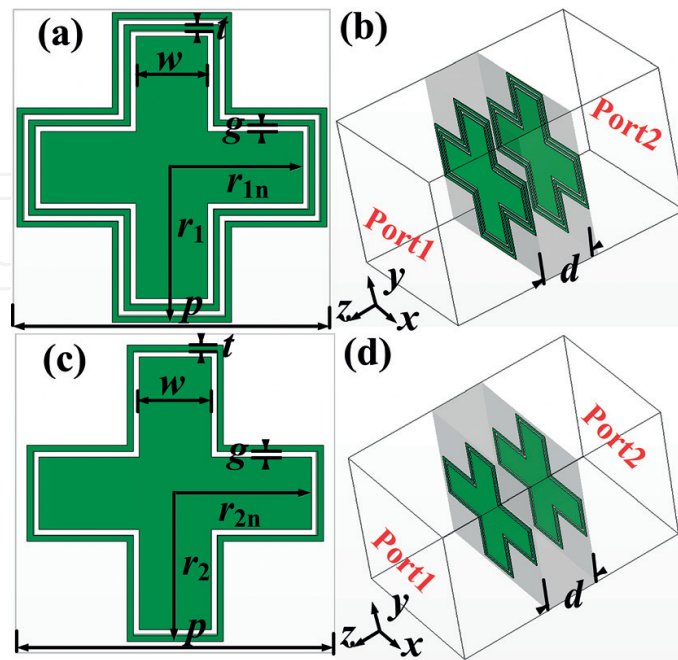
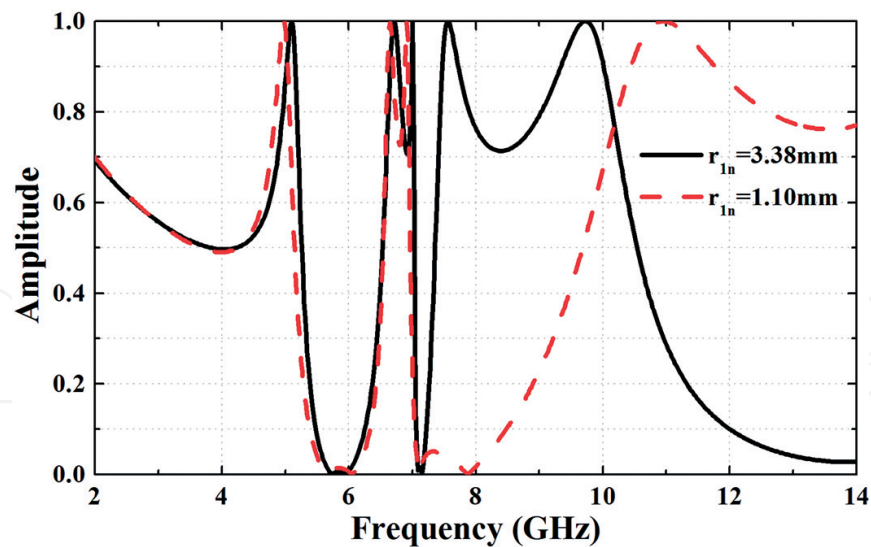


Figure 39. Structure and simulated setup of the element 1 (a, b) and element 2 (c, d).





**Figure 40.** Transmitted amplitudes of the element 1 with minimum and maximum sizes of the inner cross.

when  $r_{1n} = 3.38$  mm, there are three frequency bands, in which the transmission rate is more than 0.7. The third band is in the X band, and the transmission rate in this band changes slowly. Indeed, this resonant frequency band is mainly controlled by the cross-structure, which means that different transmitted phases at 10 GHz can be obtained by changing the cross-length ( $r_{1n}$ ). Under the requirement of the transmission efficiency over 0.7 at 10 GHz, we adjust the length  $r_{1n}$  of the cross to make the frequency point of 10 GHz fall on the rising and descending edge of the third frequency ranges. The phase changing range is shown in **Figure 41**. The difference between the minimum and the maximum transmitted phase at 10 GHz is  $204^\circ$ .

In order to achieve the phase tuning range of  $360^\circ$ , we remove the outermost cross-frame structure on the basis of CDCR element and get the second element namely the CCR element.

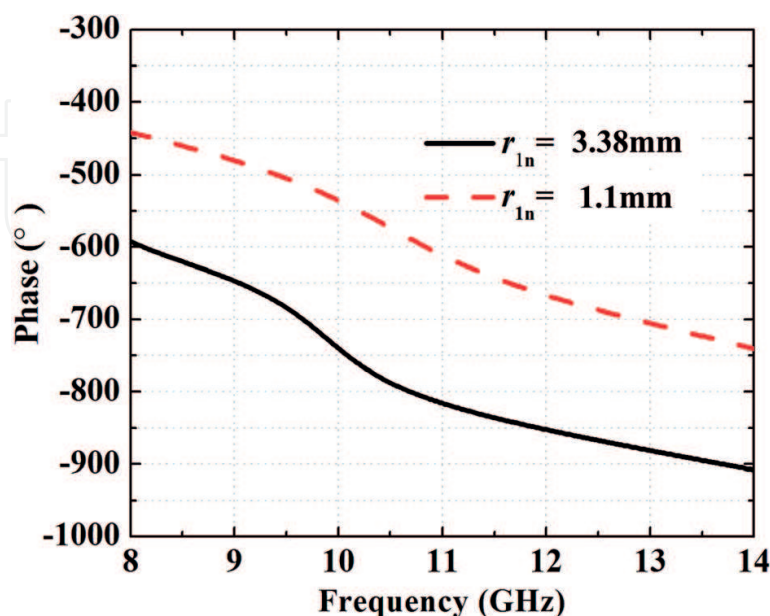


**Figure 41.** Transmitted phases of the element 1 with minimum and maximum sizes of the inner cross.

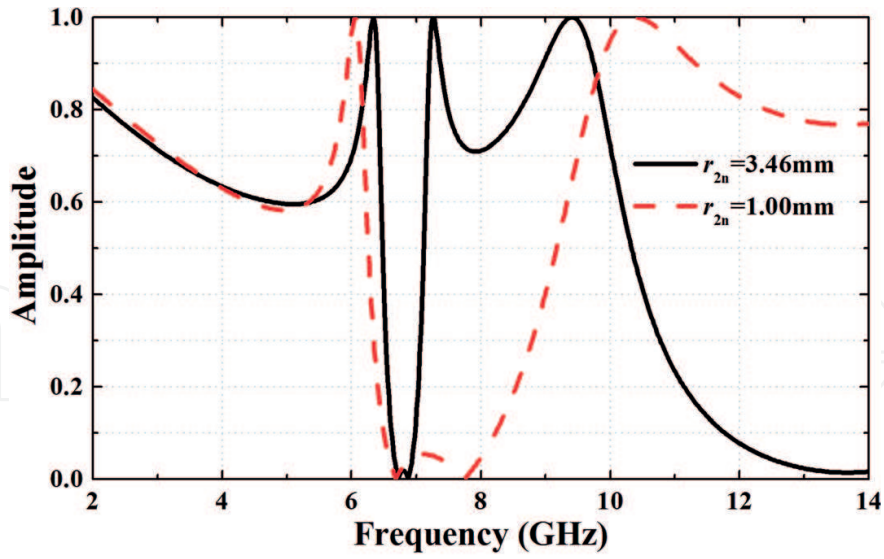


**Figure 42.** Transmitted amplitudes of the element 2 with minimum and maximum sizes of the inner cross.

To ensure that the simulated conditions are exactly the same, the size of the CCR element is slightly adjusted. When  $r_{2n}$  takes 3.46 mm and 1 mm, the curves of the transmitted amplitude are shown in **Figure 42**. The number of the frequency band, in which the transmittance is over 0.7, is reduced to two. The second resonant frequency band is mainly controlled by the cross-structure ( $r_{2n}$ ). When  $r_{2n}$  takes 3.46 mm and 1 mm, the rising and falling edges of the band fall at 10 GHz, respectively. And the corresponding transmission phase curve is shown in **Figure 43**. In combination with **Figures 41** and **43**, we find that the difference between the minimum transmission phase (absolute value) of the element 1 (CDCR element) and the maximum transmission phase (absolute value) of element 2 is  $15^\circ$  at 10 GHz, which indicates that the two elements have

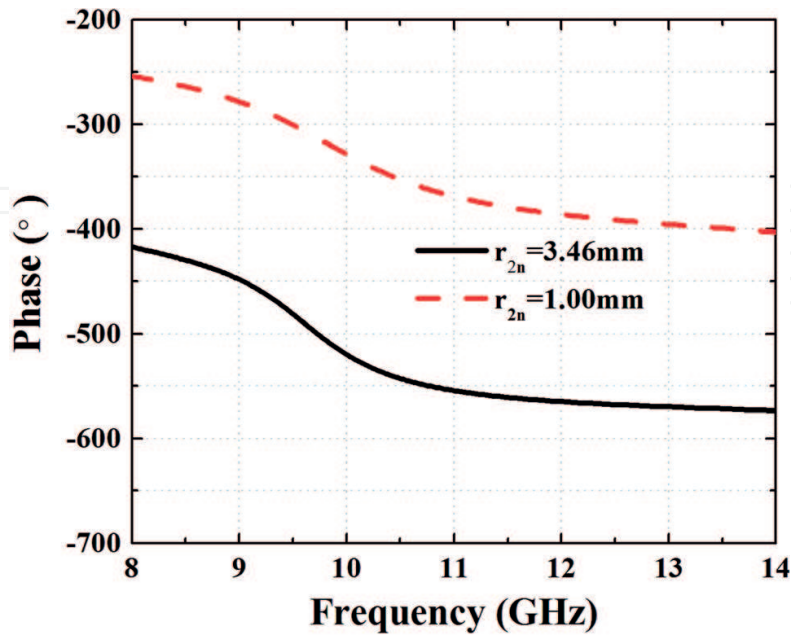


**Figure 43.** Transmitted phases of element 2 with minimum and maximum sizes of the inner cross.

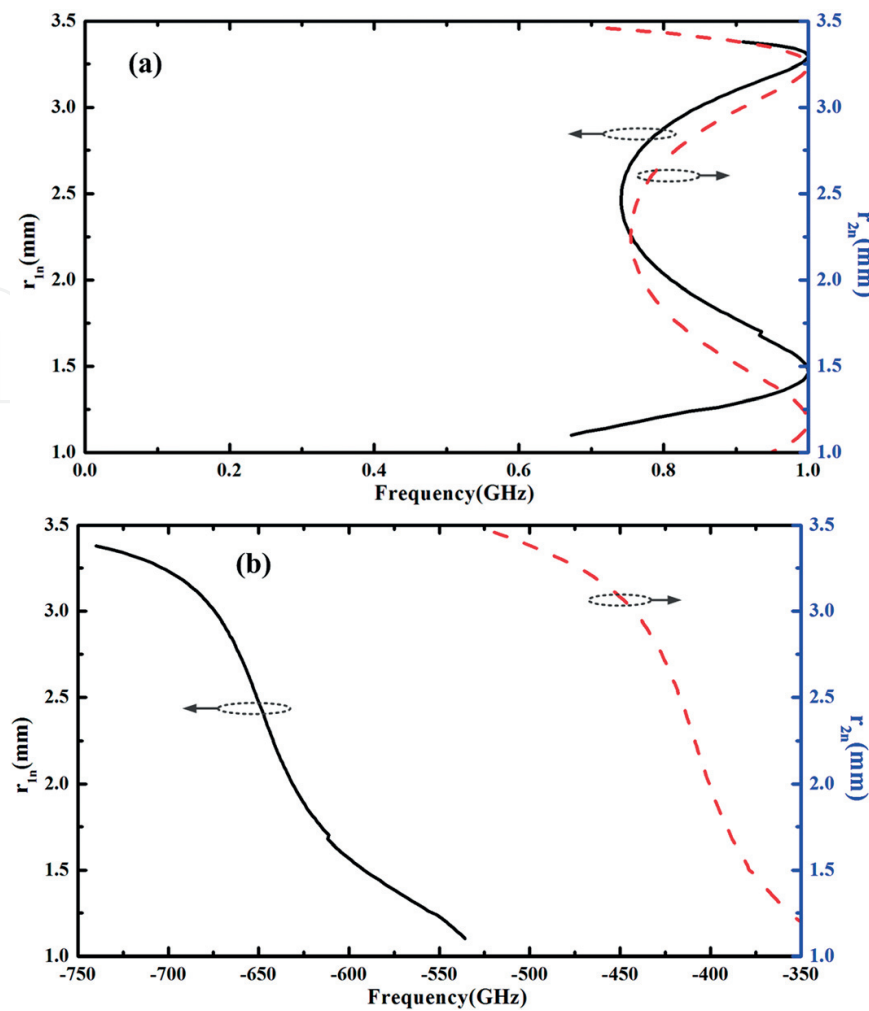


**Figure 44.** Transmission (a) phases and (b) amplitudes versus the  $r_1$  and  $r_2$  for element 1 and element 2.

achieved good phase abutment. At the same time, the  $360^\circ$  full coverage is achieved after abutting the two elements. **Figure 44** gives two curves of transmittance and transmission phase of the elements varying with their respective parameters ( $r_{1n}$  and  $r_{2n}$ ).

## 4.2. Single-layer metasurface design

From the previous analysis, it can be seen that the combination of CDCR and CCR unit cells can completely control the phase of transmitted wave under the precondition of the transmittance higher than 0.7, which meet the requirements of the transmitted focusing MS. The same as the Section 2, we use  $13 \times 13$  elements to build the transmitted MS and improve the gain of the patch antenna. According to Eq. (13), we fix  $L = 30$  mm to calculate the absolute phase distribution on MS and show it in **Figure 45(a)**, in which the transmission phase of the original point (0, 0) is  $-740^\circ$ , the element form is CDCR, the cross-parameter is  $r_{1n} = 3.38$  mm, and the value of  $k$  is reasonably selected to make the transmission phase of each unit fall within the range of  $[0, 360^\circ]$ . According to the phase distribution shown in **Figure 45(a)** and the phase distribution curve given in **Figure 44**, we can determine the unit

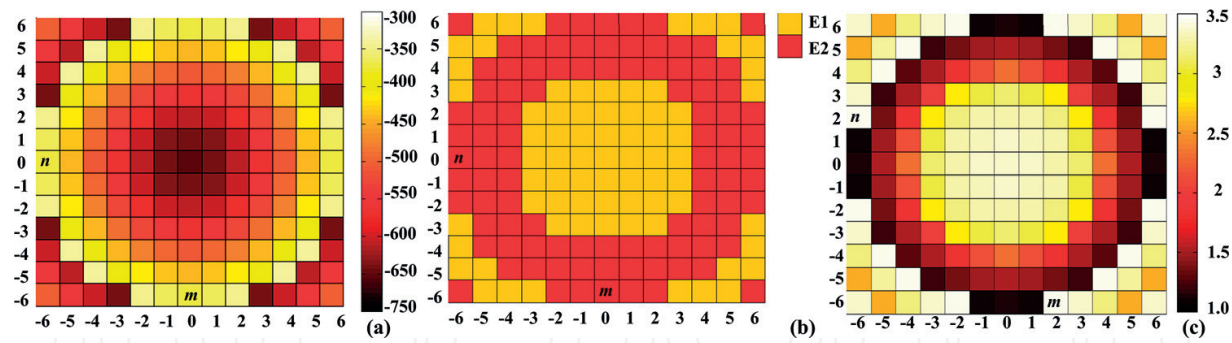


Figure 45. The (a) absolute phases, (b) element types, and (c) values of  $r_{1n}$  or  $r_{2n}$  for all the unit cells on the MS.

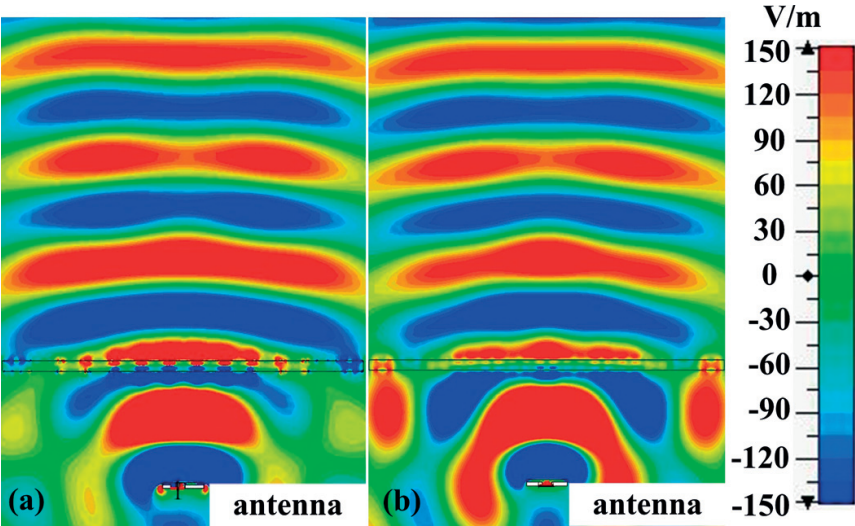


Figure 46. Simulated electric field distribution ( $E_x$ ) at 10 GHz in (a)  $xoz$ -plane and (b)  $yo$ z-plane.

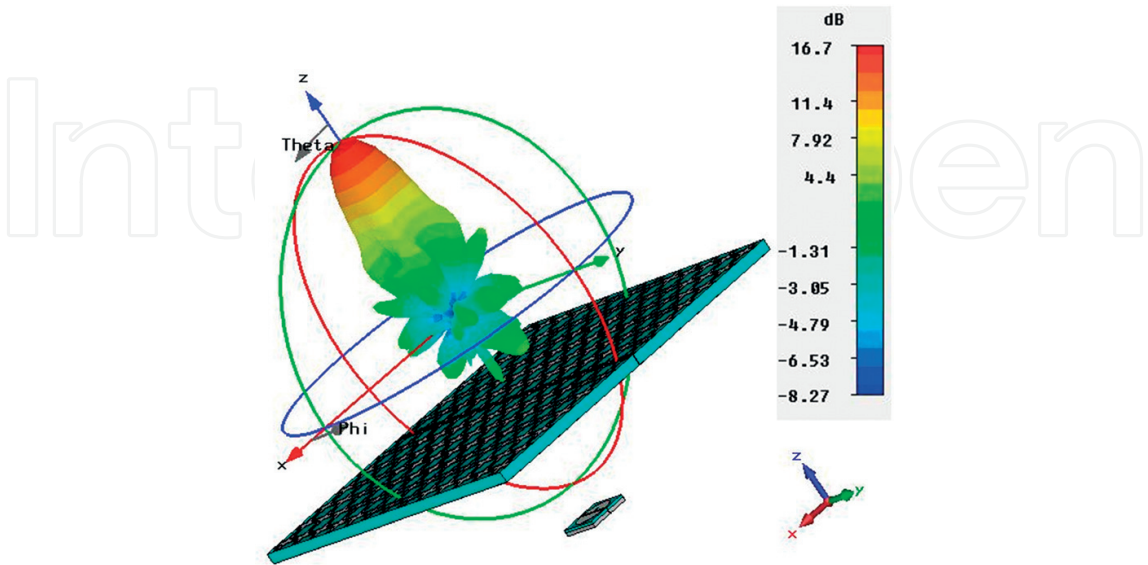
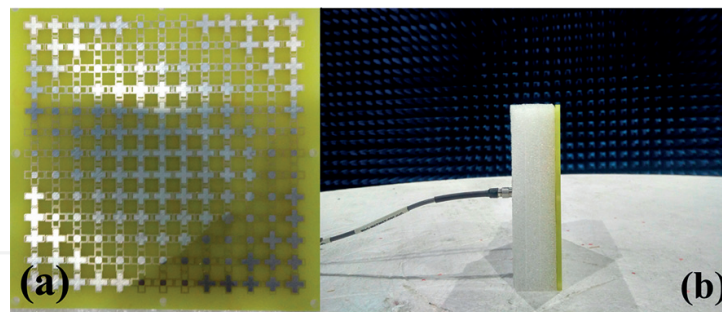


Figure 47. The (a) 3D radiation pattern at 10 GHz.





**Figure 48.** Prototype of the proposed lens antenna (a) single-layer MS and (b) the farfield measured setup.

form at every position of the MS and get the corresponding cross-parameter values. The distribution of element form is shown in **Figure 45(b)**, where red represents CDCR unit and yellow represents CCR unit. The corresponding  $r_{1n}$  or  $r_{2n}$  value distribution is shown in **Figure 45(c)**.

According to the distribution of **Figure 45(b)** and (c), a single-layer transmitted focusing MS is constructed, and the patch antenna shown in **Figure 34** is used as the feed source. **Figure 46**

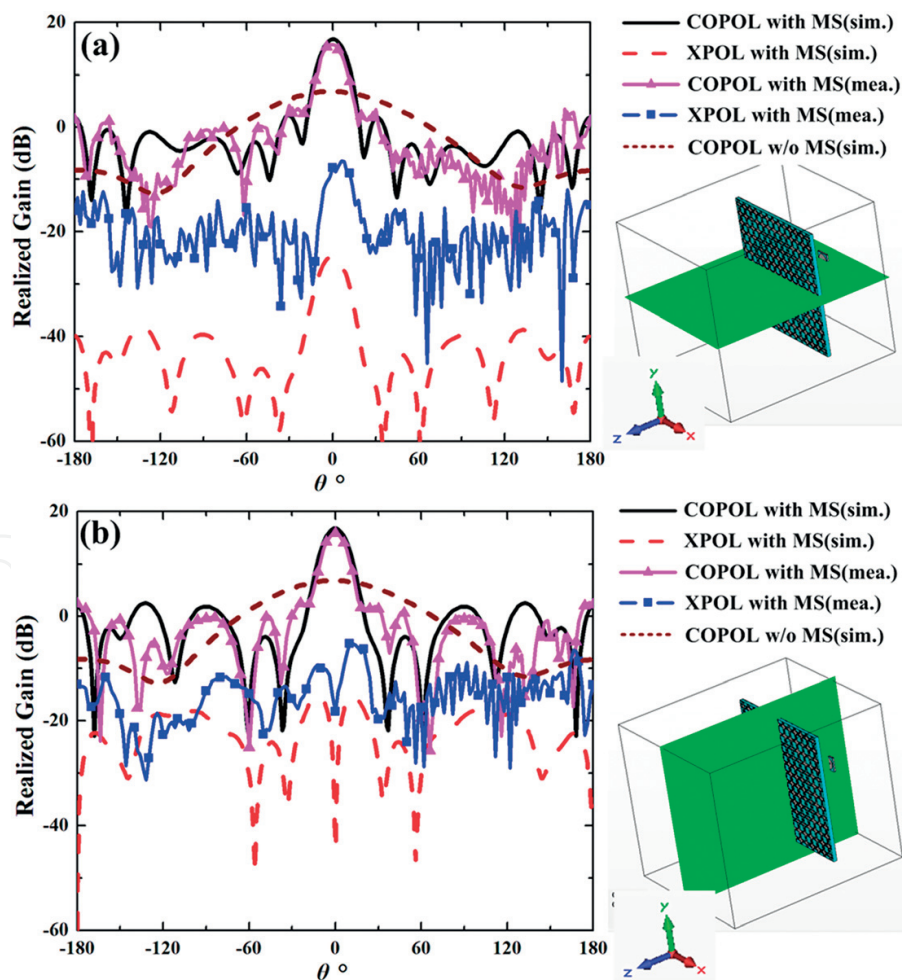


**Figure 49.** Simulated and measured 2D radiation patterns in (a)  $xoz$ -plane and (b)  $yo$  $z$ -plane.

shows the electric-field distribution at 10 GHz on the  $xoz$ - and  $yo$ z-planes. It can be seen from the figure that the spherical wave is transformed into a near-plane wave by the MS, thus increasing the gain of the feed source, as verified by the pen-shaped farfield pattern shown in **Figure 47**.

### 4.3. Lens antenna assembling and measurement

As is shown in **Figure 48**, the single-layer transmitted MS is fabricated and then assembled with a patch antenna. The lens antenna is measured in the microwave anechoic chamber. In **Figure 49**, the simulation and test patterns of the  $xoz$ - and  $yo$ z-planes at 10 GHz are given. It can be seen from the figure that the antenna gain at 10 GHz reaches 16.5 dB, which is 10 dB higher than the patch antenna, and the sidelobe level of the system is  $-15$  dB. In addition, the area of the MS is  $104 \times 104 \text{ mm}^2$ . It can be calculated that the focal-to-diameter ratio at 10 GHz is 0.29, and the aperture efficiency is about 30%.

## 5. Conclusions

In this chapter, we have reviewed our recent efforts in utilizing metasurface to enhance the gain of the conventional antenna. For reflected MS, we propose a novel single-layer unit cell to greatly widen the phase-steering range and use it to design an MS antenna which achieves a wide working band of 10–12.3 GHz. On this basis, we propose a bi-layer reflected MS to simultaneously enhance the gain and transform the linear polarization to circular polarization of the Vivaldi antenna. The new MS enhances the gain and decrease beam width of the antenna in a 3 dB axial ratio band of 9.12–10.2 GHz. While for transmitted MS, we not only try to widen the phase-tuning range but also struggle to maintain high transmissions. Two methods have been proposed in this chapter to design transmitted MS. One is based on multilayer stack and the other is using an element-group. Compared with the patch antenna, the gain enhancements at 10 GHz are 11.6 and 10 dB for the methods of multilayer stack and group-element, respectively. In addition, both of the aperture efficiencies have reached 30%. These above MS antennas not only open up a new route for the applications of focusing MSs in microwave band, but also afford an alternative for high-gain antennas.

### Author details

Haipeng Li\*, Guangming Wang\*, Wenye Ji, Tong Cai, Xiangjun Gao and Haisheng Hou

\*Address all correspondence to: s\_lihaipeng@sina.cn and wgming01@sina.com

Microwave Laboratory, Air Force Engineering University, Xi'an, China

## References

- [1] Yu NF, Genevet P, Kats MA, Aieta F, Tetienne J-P, Capasso F, Gaburro Z. Light propagation with phase discontinuities: Generalized laws of reflection and refraction. *Science*. 2011;**334**:333-337
- [2] Pors A, Nielsen MG, Eriksen RL, Bozhevolnyi SI. Broadband focusing flat mirrors based on plasmonic gradient metasurfaces. *Nano Letters*. 2013;**13**:829-834
- [3] Li X, Xiao SY, Cai BG, He Q, Cui TJ, Zhou L. Flat metasurfaces to focus electromagnetic waves in reflection geometry. *Optics Letters*. 2012;**37**:4940-4942
- [4] Aieta F, Genevet P, Kats MA, Yu NF, Blanchard R, Gaburro Z, Capasso F. Aberration-free ultrathin flat lenses and axicons at telecom wavelengths based on plasmonic metasurfaces. *Nano Letters*. 2012;**12**:4932-4936
- [5] Li H-P, Wang GM, Liang JG, Gao XJ, Hou HS, Jia XY. Single-layer focusing gradient metasurface for ultrathin planar lens antenna application. *IEEE Transactions on Antennas and Propagation*. 2017;**65**(3):1452-1457
- [6] Sun SL, Yang K, Wang C, Cui JT, et al. High-efficiency broadband anomalous reflection by gradient meta-surfaces. *Nano Letters*. 2012;**12**:6223-6229
- [7] Ni X, Emani NK, Kildishev AV, Boltasseva A, Shalaev VM. Broadband light bending with plasmonic nanoantennas. *Science*. 2012;**335**:427
- [8] Sun SL, He Q, Xiao SY, et al. Gradient-index meta-surfaces as a bridge linking propagating waves and surface waves. *Nature Materials*. 2012;**11**:426-431
- [9] Wu CJ, Cheng YZ, Wang WY, He B, Gong RZ. Ultra-thin and polarization-independent phase gradient metasurface for high-efficiency spoof surface-plasmon-polariton coupling. *Applied Physics Express*. 2015;**8**(12):122001
- [10] Zhao JM, Sima BY, Jia N, et al. Achieving flexible low-scattering metasurface based on randomly distribution of metaelements. *Optics Express*. 2016;**24**(2):27850
- [11] Song Y-C, Ding J, Guo C-J, Ren Y-H, Zhang J-K. Ultra-broadband backscatter radar cross section reduction based on polarization-insensitive metasurface. *IEEE Antennas and Wireless Propagation Letters*. 2016;**15**:329-331
- [12] Liu Y, Li K, Jia YT, Hao YW, Gong SX, Guo YJ. Wideband RCS reduction of a slot array antenna using polarization conversion metasurfaces. *IEEE Transactions on Antennas and Propagation*. 2016;**64**(1):326-331
- [13] Li HP, Wang GM, Wang JG, Gao XJ. Wideband multifunctional metasurface for polarization conversion and gain enhancement. *Progress in Electromagnetics Research*. 2016;**155**:115-125
- [14] Song K, Liu YH, Luo CR, Zhao XP. High-efficiency broadband and multiband cross-polarization conversion using chiral metamaterial. *Journal of Physics D: Applied Physics*. 2014;**47**:505104



- [15] Yang YM, Wang WY, Moitra P, Kravchenko II, Briggs DP, Valentine J. Dielectric meta-reflectarray for broadband linear polarization conversion and optical vortex generation. *Nano Letters*. 2014;**14**:1394-1399
- [16] Grady NK, Heyes JE, Chowdhury DR, Zeng Y, et al. Terahertz metamaterials for linear polarization conversion and anomalous refraction. *Science*. 2013;**340**:1304-1306
- [17] Zhu L, Meng F-Y, Dong L, Fu J-H, Zhang F, Wu Q. Polarization manipulation based on electromagnetically induced transparency-like (EIT-like) effect. *Optics Express*. 2013;**21**(26):32100-32110
- [18] Chen HY, Wang JF, Ma H, Qu SB, Xu Z, Zhang AX, Yan MB, Li YF. Ultra-wideband polarization conversion metasurfaces based on multiple plasmon resonances. *Journal of Applied Physics*. 2014;**115**:154504
- [19] Ma HF, Wang GZ, Kong GS, Cui TJ. Broadband circular and linear polarization conversions realized by thin birefringent reflective metasurfaces. *Optical Materials Express*. 2014;**4**(8):1718-1724
- [20] Yoon JH, Kim JS, Yoon YJ, Lee WS, So JH. Single-layer reflectarray with combination of element types. *Electronics Letters*. 2014;**50**(8):574-576